Journal of Geochemical Exploration 241 (2022) 107060

Contents lists available at ScienceDirect

Journal of Geochemical Exploration

journal homepage: www.elsevier.com/locate/gexplo

Late Triassic granitic magmatism and tungsten mineralization in NE China: Geochronological and geochemical constraints from the Tantoushan quartz-wolframite vein-type deposit

Wei Xie [a,b,c], Qing-Dong Zeng [a,b,c,*], Ling-Li Zhou [d], Ting-Guang Lan [e], Rui-Liang Wang [f], Jin-Jian Wu [a,b,c]

[a] *Key Laboratory of Mineral Resources, Institute of Geology and Geophysics, Chinese Academy of Sciences, Beijing 100029, China*
[b] *Innovation Academy for Earth Science, Chinese Academy of Sciences, Beijing 100029, China*
[c] *College of Earth and Planetary Sciences, University of Chinese Academy of Sciences, Beijing 100049, China*
[d] *Earth and Ocean Sciences and Irish Centre for Research in Applied Geosciences (iCRAG), National University of Ireland, Galway H91TK33, Ireland*
[e] *State Key Laboratory of Ore Deposit Geochemistry, Institute of Geochemistry, Chinese Academy of Sciences, Guiyang 550081, China*
[f] *Faculty of Geosciences and Resources, China University of Geosciences (Beijing), Beijing 100083, China*

A R T I C L E I N F O

Keywords:
Zircon U-Pb age
Wolframite *in situ* U-Pb age
Zircon Hf isotopes
Wolframite geochemistry
Tantoushan W deposit
NE China

A B S T R A C T

NE China, located at the eastern Central Asian Orogenic Belt, experienced extensive magmatism during the Mesozoic and hosts multistage granitic plutons and accompanying W mineralization. However, due to the limited number of studies on Triassic W deposits and spatially related granitoids, the petrogenesis of these granitoids and their relation to W mineralization remain enigmatic. The Tantoushan quartz-wolframite vein-type deposit is located on the southern margin of NE China. Tungsten mineralization occurs mainly in the veins and veinlets within monzogranites. A lower intercept $^{206}Pb/^{238}U$ age of 234.3 ± 6.2 Ma (1σ, MSWD = 0.41) was obtained for wolframite, which is identical within uncertainties to the zircon weighted mean $^{206}Pb/^{238}U$ age of 233.1 ± 1.8 Ma (1σ, MSWD = 0.41) from the W-bearing monzogranites. The monzogranites have the petrological, mineralogical, and geochemical characteristics of highly fractionated I-type granitoids. The rocks are enriched in Rb, Th, U, K, and Pb, and depleted in Ba, Sr, P, and Ti. They have higher W concentrations and Rb/Sr ratios, and lower Nb/Ta, Zr/Hf, and K/Rb ratios than the contemporary W-barren granitoids in NE China. These geochemical characteristics and negative zircon $\varepsilon_{Hf}(t)$ values (−17.7 to −8.6), as well as old two-stage model ages (T_{DM2} = 1807–2378 Ma), suggest that the monzogranites were derived as a product of the partial melting of the Paleoproterozoic lower crust and subsequently underwent extreme fractional crystallization. Geochronological and geochemical evidence collectively suggest that the W mineralization in the Tantoushan deposit is genetically related to the W-bearing monzogranites, and extreme fractional crystallization was essential for W enrichment in the granitic magma. In contrast, Triassic W-barren granitoids did not induce W mineralization, probably because of their low fractionated signatures. We preliminarily demonstrate that an isovalent substitution mechanism of $4^{A}(Fe, Mn)^{2+} + 8^{B}W^{6+} + {}^{B}\square \leftrightarrow 3^{A}M^{3+} + {}^{A}N^{4+} + 7^{B}(Nb, Ta)^{5+} + 2^{B}N^{4+}$ played a critical role in the formation of hydrothermal wolframite in the Tantoushan deposit, and the trace elements compositions of wolframite were controlled by both the crystallochemical parameters and composition of the initial hydrothermal fluids. In the context of the regional geology, we propose that the Tantoushan monzogranites and corresponding W mineralization were formed in a post-collision extensional setting controlled by the closure of the Paleo-Asian Ocean during the Late Triassic. In combination with previous studies, we suggest that NE China may have enormous potential for Triassic W mineralization and the Triassic highly fractionated granitoids distributed on both sides of the Solonker-Xar Moron-Changchun Fault represent potential targets for future exploration of additional W resources.

* Corresponding author at: Key Laboratory of Mineral Resources, Institute of Geology and Geophysics, Chinese Academy of Sciences, Beijing 100029, China.
E-mail address: zengqingdong@mail.iggcas.ac.cn (Q.-D. Zeng).

https://doi.org/10.1016/j.gexplo.2022.107060
Received 15 November 2021; Received in revised form 15 July 2022; Accepted 27 July 2022
Available online 2 August 2022

1. Introduction

NE China, tectonically known as the Xing-Meng Orogenic Belt (XMOB), comprises the main part of the eastern segment of the Central Asian Orogenic Belt (CAOB) and represents one of the most important polymetallic metallogenic provinces in China (Zeng et al., 2011, 2012, 2015a; Ouyang et al., 2013, 2015; Wang et al., 2021; Xie et al., 2021a, 2021b) (Fig. 1). Numerous W deposits have been discovered in this region, demonstrating its significant W metallogenic potential (Ouyang et al., 2015; Zeng et al., 2015b; Liu et al., 2016; Wang et al., 2017, 2020a, 2021; Zhang et al., 2017a; Gao et al., 2019; Xie et al., 2021b). To date, NE China is known to host 4 large, 18 medium, and 17 small W deposits (Fig. 1c). These deposits have a combined total resource of >0.62 Mt. (Xie et al., 2021b). Three W belts were distinguished based on the spatial distribution of W deposits, namely the northern and central Great Xing'an Range W belt, the southern Great Xing'an Range W belt (SGB), and the Lesser Xing'an-Zhangguangcai Range W belt, respectively (Wang et al., 2021; Xie et al., 2021b) (Fig. 1c). Geochronologically, three episodes of W mineralization were recognized in this region, including Triassic (240–250 Ma), Early–Middle Jurassic (170–200 Ma), and Late Jurassic–Early Cretaceous (125–160 Ma) (Xie et al., 2021b). Previous studies have mainly focused on the Jurassic and Early Cretaceous W mineralization (Shao et al., 2011; Yang et al., 2012, 2013, 2019; Hao et al., 2013; Zeng et al., 2015b; Guo et al., 2016; Li et al., 2016a, 2016b; Xiang et al., 2016a, 2016b, 2018; Chen et al., 2017; Shang et al., 2017; Wang et al., 2018, 2020a; Gao et al., 2019; Xie et al., 2022b). In contrast, only a few studies have been conducted on Triassic W deposits (Zhao, 2014; Peng et al., 2015). This knowledge gap impedes our understanding of the regional W metallogeny. In addition, the W deposits in NE China are often spatially associated with Mesozoic granitic intrusions (Hu et al., 2006, 2014; Guo et al., 2014; Jiang et al., 2016; Yang et al., 2016; Zhang et al., 2016; Wang et al., 2017, 2021; Fei et al., 2018; Li et al., 2019; Xie et al., 2022b). However, owing to a paucity of studies carried out on the Triassic W-bearing granites, their petrogenesis and relation to W mineralization remains poorly understood. In most cases, spatially associated granitoids are interpreted to be the sources of ore-forming materials (e.g., Refy, 1997; Audétat et al., 2000; Webster et al., 2004; Hulsbosch et al., 2016; Korges et al., 2018; Pan et al., 2019; Li et al., 2020). In contrast, another perspective is that the spatially related granitoids may have only served as the country rocks of W deposits and are not genetically related to W mineralization (e.g., Dewaele et al., 2016; Lecumberri-Sanchez et al., 2017; Cao et al., 2018a; Yuan et al., 2018; Xiong et al., 2020; Feng et al., 2021; Li et al., 2021b). Advanced by recent developments in *in situ* U-Pb dating and geochemical analytical techniques on wolframite, it is now possible to constrain the age of W mineralization in great precision and understand the metal precipitation process in great details (e.g., Harlaux et al., 2018; Zhang et al., 2018; Deng et al., 2019; Tang et al., 2020; Xiong et al., 2020; Yang et al., 2020, 2022; Carr et al., 2021; Li et al., 2021b; Xie et al., 2022a). In combination with the geochronology and geochemistry methods used for W-bearing granites, the genetic link between the W-bearing granites and W mineralization can now be addressed. This approach is particularly important in the context of NE China, where the Triassic W-bearing and W-barren granitoids commonly coexist and the difference between their geochemical signatures remains ambiguous due to limited number of studies.

It is well understood that the tectonic evolution of NE China was critical for the spatial and temporal distribution of W deposits and related granites. Romer and Kroner (2016) conclude that different tectonic settings might have led to the input of mantle melt or the emplacement of ultrahigh-temperature metamorphic rocks. These were essential for metal extraction from the source rocks and thus played a critical role in controlling the discontinuous distribution of W mineralization within metallogenic belts. However, the tectonic setting of NE China during the Triassic is still debated. Although researchers generally agree that the disappearance of the Paleo-Asian Ocean (PAO) occurred along the Solonker-Xar Moron-Changchun Fault (SXCF), the closure time of the PAO remains controversial (Eizenhöfer et al., 2014; Liu et al., 2017). There are two different suggestions, including a widely accepted one which suggests the closure occurred during the Late Permian to Early Triassic (Zhai and Santosh, 2013; Xiao and Santosh, 2014; Han et al., 2015; Liu and Nie, 2015; Wilde, 2015), and the another which dates the closure to the pre-Permian period (Zhang et al., 2008b; Shi et al., 2010; Xu et al., 2013a; Li et al., 2014b; Xu et al., 2015). These two different suggestions lead to two different scenarios of tectonic setting for the Triassic W mineralization and magmatism. Hence, determining the tectonic setting of Triassic W-related granites and associated W deposits is important to understand the petrogenesis of W-related granitic magmatism and the genesis of W deposits at a regional scale, providing novel guidelines for future W exploration.

The Tantoushan W deposit, located on the southern margin of the XMOB, is a typical quartz-wolframite vein-type deposit. It represents an important hydrothermal W mineralization event. W mineralization occurs mainly in veins and veinlets within monzogranites. However, owing to the paucity of detailed petrographic, geochronological, and geochemical studies, the precise age of magmatism and mineralization, petrogenesis of monzogranite, and the possible genetic link between magmatism and W mineralization remain unclear. In this contribution, we report a high-quality zircon U-Pb age, whole-rock geochemical data, and zircon Hf isotope compositions of the W-bearing monzogranites, as well as *in situ* U-Pb age and geochemical data of wolframite. The aims of this study are to: (1) precisely constrain the timing of monzogranite emplacement and W mineralization; (2) decipher the petrogenesis of the Tantoushan W-bearing monzogranite and its geochemical differences as compared with contemporary W-barren granitoids in NE China; (3) examine the factors controlling the trace element compositions of wolframite; and (4) clarify the genetic link between the W-bearing monzogranites and W mineralization in the Tantoushan deposit. In combination with previous studies, we further constrain the metallogenic tectonic settings of NE China in the Late Triassic and provide new guidelines for future W exploration in the region.

2. Geological setting

NE China is composed of a collage of microcontinental blocks, including, from northwest to southeast, the Erguna Block, Xing'an Block, Songliao-Xilinhot Block, Khanka-Jiamusi Block, and the Liaoyuan Terrane in the southernmost areas (Wu et al., 2011; Liu et al., 2017) (Fig. 1). The Xinlin-Xiguitu Fault represents the boundary between the Erguna and Xing'an blocks, the Hegenshan-Heihe Fault separates the Xing'an and Songliao-Xilinhot blocks, the Mudanjiang Fault represents the boundary between the Songliao-Xilinhot and Khanka-Jiamusi blocks, and the SXCF is generally considered as the boundary between the Songliao-Xilinhot Block and Liaoyuan Terrane (Wu et al., 2011; Liu et al., 2017) (Fig. 1). Throughout the Phanerozoic, the XMOB underwent complex tectonic-magmatic evolutionary processes that involved multiple stages of accretion and collision (Sengör et al., 1993). During the Paleozoic, the XMOB was controlled by the PAO tectonic regime, which led to the amalgamation of several microcontinental blocks, multi-arc systems, and accretionary complexes (Wu et al., 2011; Xiao and Santosh, 2014; Zhang et al., 2022). After the scissor-type closure of the PAO that occurred during the Late Permian–Middle Triassic period along the SXCF, the microcontinental blocks of NE China amalgamated. The North China Craton (NCC) collided with the Siberian Craton (SC) along the northern margin after the closure of the Mongol-Okhotsk Ocean from the latest Early Mesozoic to the Late Mesozoic in a scissor-like style from west to east (Zorin, 1999; Eizenhöfer et al., 2014). Moreover, since the Mesozoic, the tectonic regime of NE China was superimposed by the northwestern subduction of the Paleo-Pacific Ocean plate beneath the Eurasian continent (Wu et al., 2011; Ma et al., 2017). The superimposed effects of several tectonic regimes led to the widespread occurrence of Mesozoic granitic intrusions and associated deposits (Wu et al., 2011;

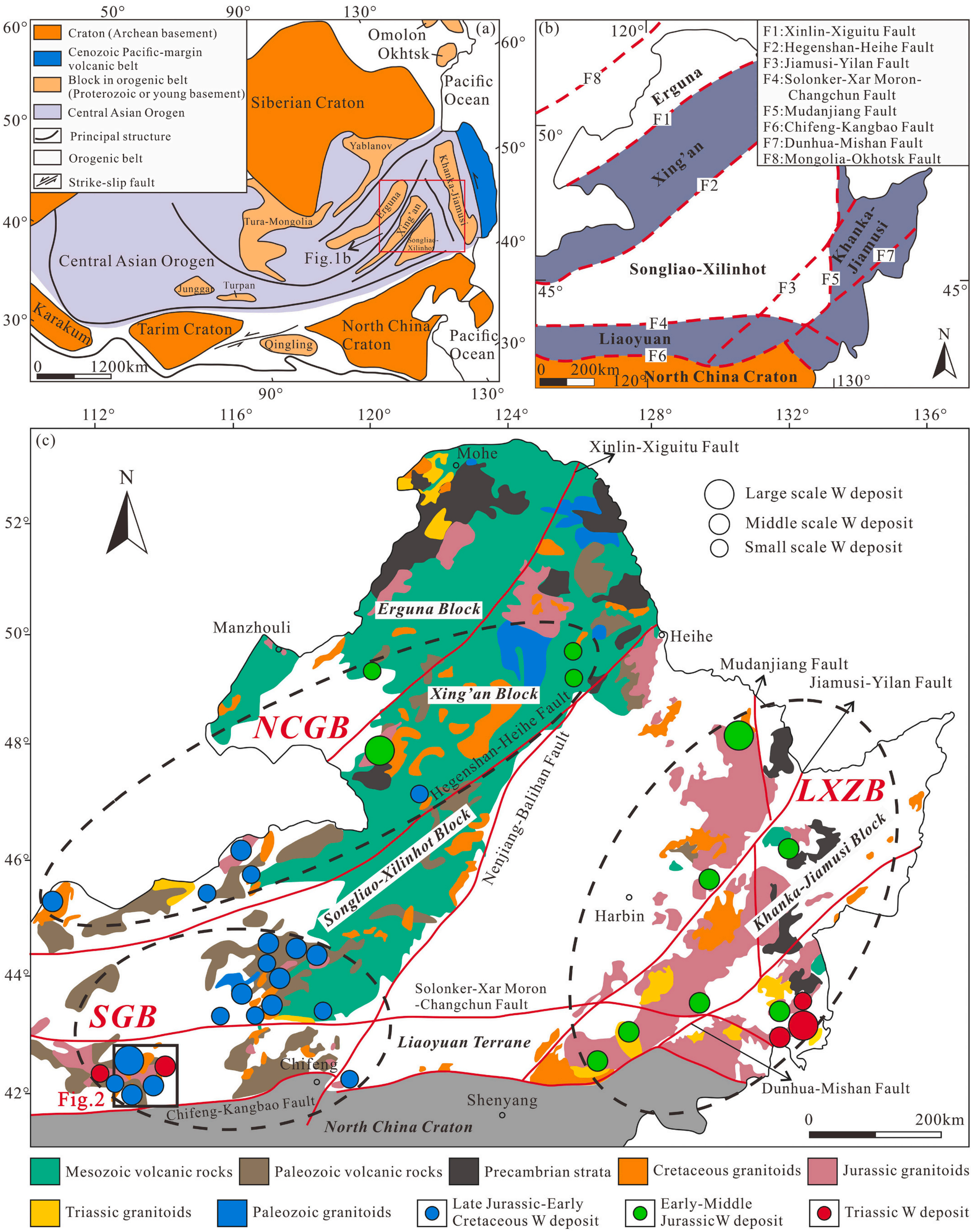

Fig. 1. (a) simplified tectonic map of the Central Asian Orogenic Belt (modified from Feng et al., 2019; Liu et al., 2017). (b) schematic tectonic map of NE China (modified from Wu et al., 2011). (c) distribution of major tungsten deposits in NE China (modified from Zeng et al., 2012). Abbreviations are as follow: NCGB = the northern and central Great Xing'an Range W belt; SGB = the southern Great Xing'an Range W belt; LXZB = the Lesser Xing'an-Zhangguangcai Range W belt.

Zeng et al., 2012, 2015a; Ouyang et al., 2013, 2015; Liu et al., 2017; Wang et al., 2021; Xie et al., 2021b; Chen et al., 2022).

The SGB, located in the southwestern part of NE China, extends north to the Heilongjiang and Jilin provinces and east to the Songliao Basin. The northern, southern, and eastern parts of the SGB are bounded by the Hegenshan-Heihe, Chifeng-Kangbao, and Nenjiang-Balihan faults, respectively (Wang et al., 2021; Xie et al., 2021b) (Fig. 1c). The SGB contains early Paleozoic marine sedimentary and late Paleozoic to early Mesozoic marine and marine-continental sedimentary units, including the Permian Dashizhai, Zhesi, and Linxi formations, and the Early Triassic Laolongtou formations (IMBGMR, 1991). Widespread Mesozoic volcanic rocks have been subdivided, from oldest to youngest, into the Manketouebo, Manitu, Baiyingaolao, and Meiletu formations (IMBGMR, 1991). Voluminous Late Paleozoic to Mesozoic granitic plutons intruded into the Paleozoic strata, which were overlain by Mesozoic volcano-sedimentary sequences. Recent geochronological data suggest that the granitic magmatic events within the SGB occurred in two stages (Wu et al., 2011). During the first stage, Late Paleozoic intrusions, comprising diorites, tonalites, and granodiorites, were mainly emplaced throughout the western part of the region and yielded U-Pb zircon ages of 321–250 Ma (Fig. 1c). During the second stage, emplacement of Mesozoic granites comprising granodiorites, monzogranites, and granite porphyries occurred, evidenced by the zircon U-Pb ages of 150–131 Ma (Wu et al., 2011; Wan et al., 2019).

The Narenwula ore field in the southwestern SGB features large-scale W polymetallic mineralization (Fig. 2). To date, one large-scale (Narenwula) and four middle-scale (Baishitouwa, Shazigou, Sansheng, and Tantoushan) W deposits have been discovered, demonstrating significant W metallogenic potential. In this region, Proterozoic–Early Paleozoic leptite, granulite, metasandstone, slate, phyllite, schist, and crystalline limestone are locally exposed. The Lower Permian and Jurassic strata are widely exposed, comprising intermediate–felsic

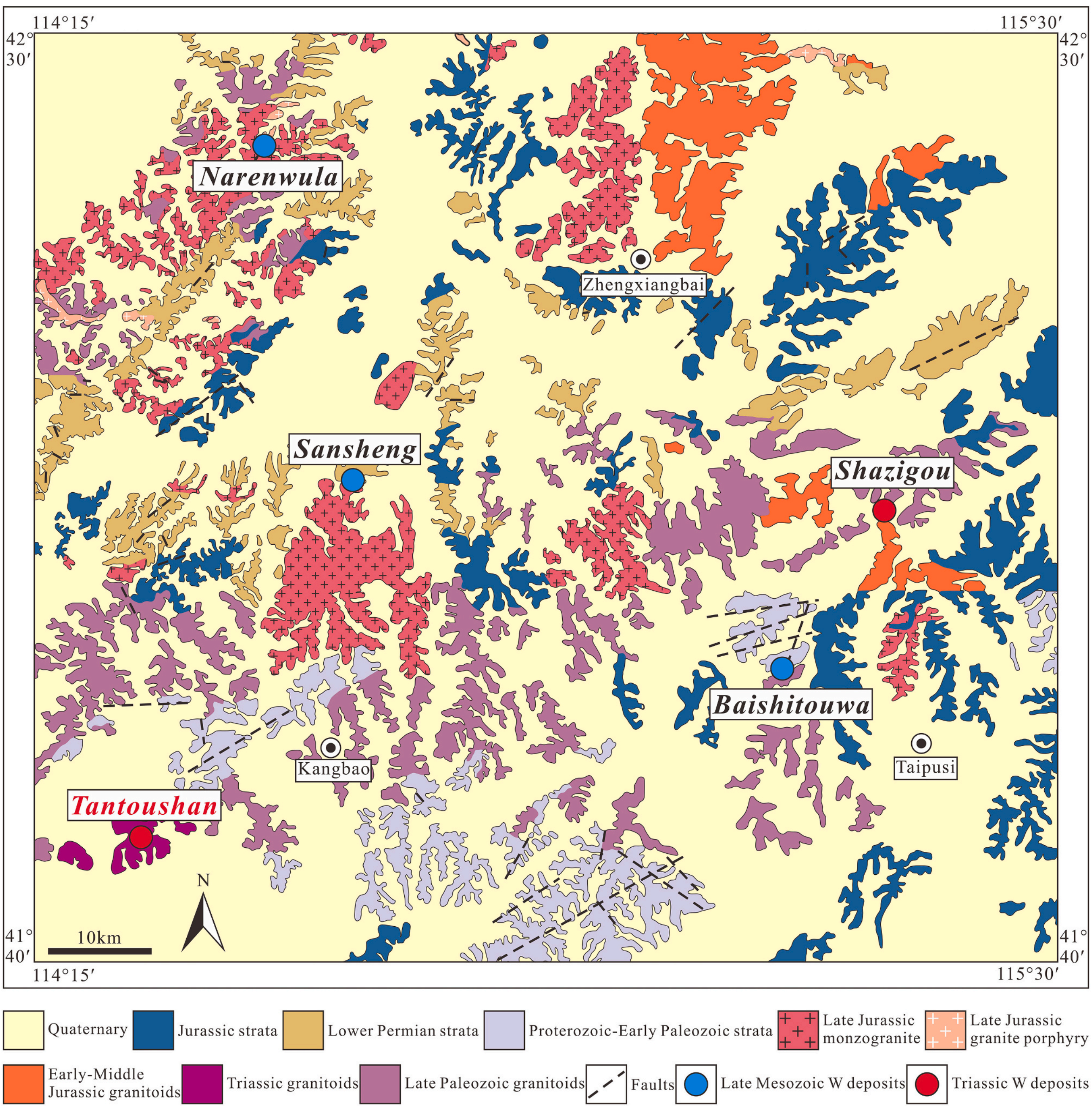

Fig. 2. Simplified geological map of the Narenwula ore field (after IMBGMR, 1991).

volcanic rocks, volcaniclastic rocks, and sedimentary clastic rocks (IMBGMR, 1991). The intrusive rocks include Late Permian, Triassic, Early-Middle Jurassic, and Late Jurassic granitic intrusions. The Late Permian felsic intrusive rocks intruded into the Proterozoic–Early Paleozoic strata, which mainly include granodiorites and quartz diorites. A Triassic granitic pluton is locally exposed in the southwestern part of this region. The Early–Middle Jurassic granitoids, which comprise fine-grained granite and minor biotite granite, occur mainly in the western part of the region, with minor occurrences in the eastern part. The Late Jurassic granitoids are common in the central and western parts of this region and mainly comprise monzogranites and granite porphyries (IMBGMR, 1991) (Fig. 2).

3. Deposit geology

The Tantoushan quartz-wolframite vein-type deposit (114°21′E, 41°46′N) is located 20 km southwest of Kangbao County (Fig. 2). The deposit contains estimated reserves of 16,500 t WO_3 with a grade of 0.343 %. The Lower Permian metamorphic rocks, comprising granitic gneiss, monzonite gneiss, mica schist, and magnetite quartzite, are locally exposed in the northwestern part of the mining area (Pan, 2010). A series of NE- and NNE-trending faults are developed in the district. Among them, the NNE-trending faults that develop within the W-bearing monzogranite are the main ore-controlling structures, which dip to the southeast at an angle of 70–90° (Fig. 3). The widespread Late Triassic monzogranites in the region are the main host rocks of W mineralization in this area (Fig. 3). The monzogranite is red in colour and displays a hypidiomorphic granular texture and massive structure (Fig. 4a–f). It consists of quartz (1–2.5 mm in length; 30–40 vol%), alkali feldspar (1.5–2.5 mm, 25–35 vol%), plagioclase (0.8–1.4 mm; 15–20 vol %), and biotite (1–1.5 mm, 5–10 vol%), along with minor accessory minerals.

Eleven ore bodies were identified in the mining district, most of which are distributed along the NNE-trending faults (Fig. 3). The ore bodies occur as parallel ore-bearing quartz veins, which dip to the SE at an angle 70–90° and are 60–340 m in length and 0.1–2.7 m in thickness. The main ore bodies are named as Nos. 1 and 2, which dip at an angle of 70–80° towards 100–112°, and are 200–340 m in length and 0.2–2.7 m in thickness (Fig. 3). W mineralization occurs as veins and veinlets, with a minor amount in dissemination (Fig. 5a–c). The burial depth of the main ore veins is relatively small and is controlled by a series of exploration trenches. The orebodies are currently mined in an open pit. Future exploration work at depth will focus on understanding the genetic link between W-bearing monzogranites and W mineralization in this area. The main ore minerals are wolframite, pyrite, chalcopyrite, galena, sphalerite, and arsenopyrite (Fig. 5f–l). Wolframite is characterized by medium- and coarse-grained anhedral to subhedral crystals (Fig. 5f). Backscattered electron (BSE) images show that wolframite is homogeneous without significant alteration (Fig. 5g). It is often intergrown with quartz (Fig. 5a, b) and is commonly superimposed by late metal sulfides (Fig. 5c). Arsenopyrite appears as rhomboid euhedral crystals and is often replaced by chalcopyrite (Fig. 5h). Pyrite is present

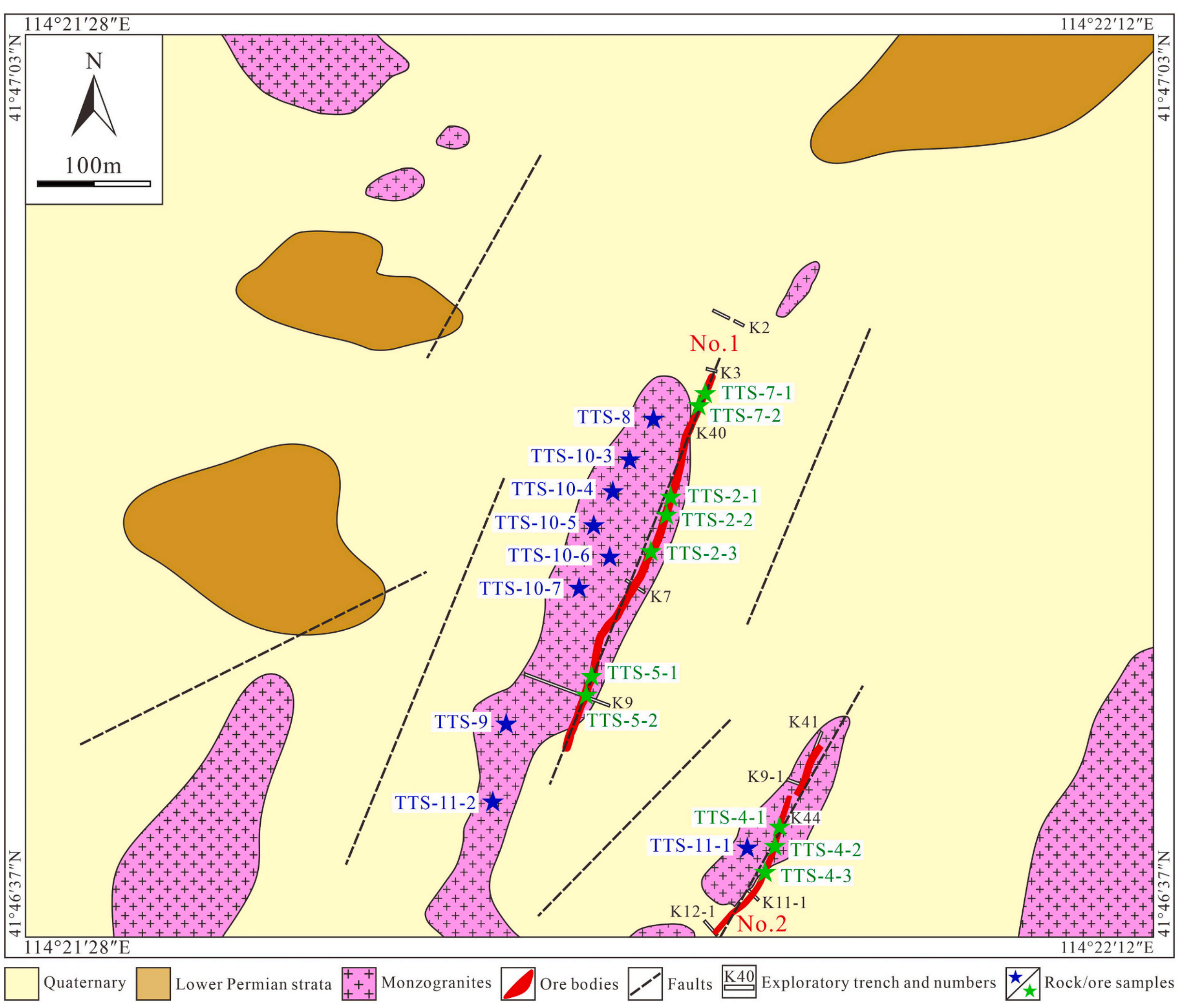

Fig. 3. Sketch geological maps of the Tantoushan W deposit (after Pan, 2010).

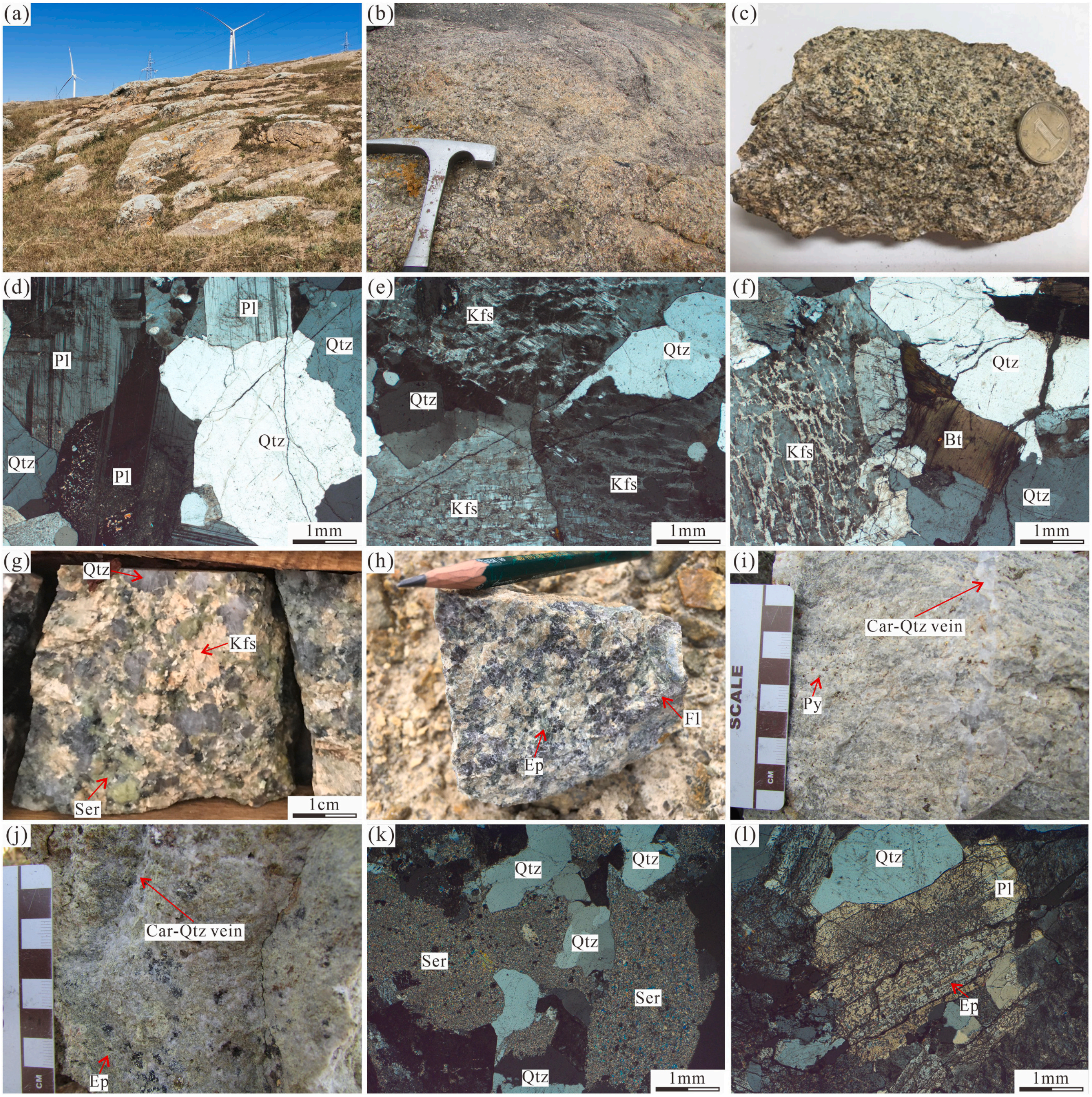

Fig. 4. Representative photographs for lithologic characteristics of monzogranite (a–f) and wall-rock alteration (g–l) in the Tantoushan W deposit (photomicrographs are under crossed-polarized light). (a, b) field outcrop of monzogranite; (c) hand specimen photographs of the monzogranite; (d, e, f) Photomicrographs showing hypidiomorphic granular texture of monzogranite; (g) K-feldspathization, silicification, and sericitization; (h) Fluoritization and epidotization; (i) Carbonate and quartz veins in altered monzogranite; (j) Carbonate and quartz veins and epidotization in monzogranite; (k) Sericite replacing plagioclase; (l) Plagioclase replaced by epidote. Abbreviations: Qtz: quartz; Kfs: potassium feldspar; Pl: plagioclase; Bt: biotite; Ser, sericite; Ep, epidote; Fl, fluorite; Car, carbonate; Py, pyrite.

as coarse-grained euhedral to subhedral crystals. It is often fragmentary and replaced by chalcopyrite and sphalerite along fractures and crystal margins (Fig. 5i, j). Sphalerite is medium-grained (1–2 mm) with an irregular shape and coexists with pyrite, chalcopyrite, and galena (Fig. 5j–l). The exsolution texture of the sphalerite-chalcopyrite solid solution is common (Fig. 5j, k). Chalcopyrite is fine- (<0.05 mm) to medium-grained (1–1.5 mm) and irregularly shaped (Fig. 5j, k). Medium-grained chalcopyrite is observed to have replaced sphalerite along the margin, indicating that it was formed later than sphalerite and fine-grained chalcopyrite (Fig. 5k). Galena is intergrown with sphalerite, and the contact boundary between galena and sphalerite is commonly smooth (Fig. 5l). The gangue minerals are quartz, K-feldspar, sericite, fluorite, epidote, and calcite. Based on a field investigation of the crosscutting relationships combined with microscopic observations of mineral assemblages and paragenetic sequences, we can divide the mineralization of the Tantoushan W deposit into three stages, which are stage I of quartz-wolframite, stage II of quartz-polymetallic sulfides, and stage III of quartz-carbonate-fluorite. Stage I mineralization is dominated by quartz and wolframite. Stage II is characterized by abundant sulfides, including pyrite, galena, sphalerite, chalcopyrite, and

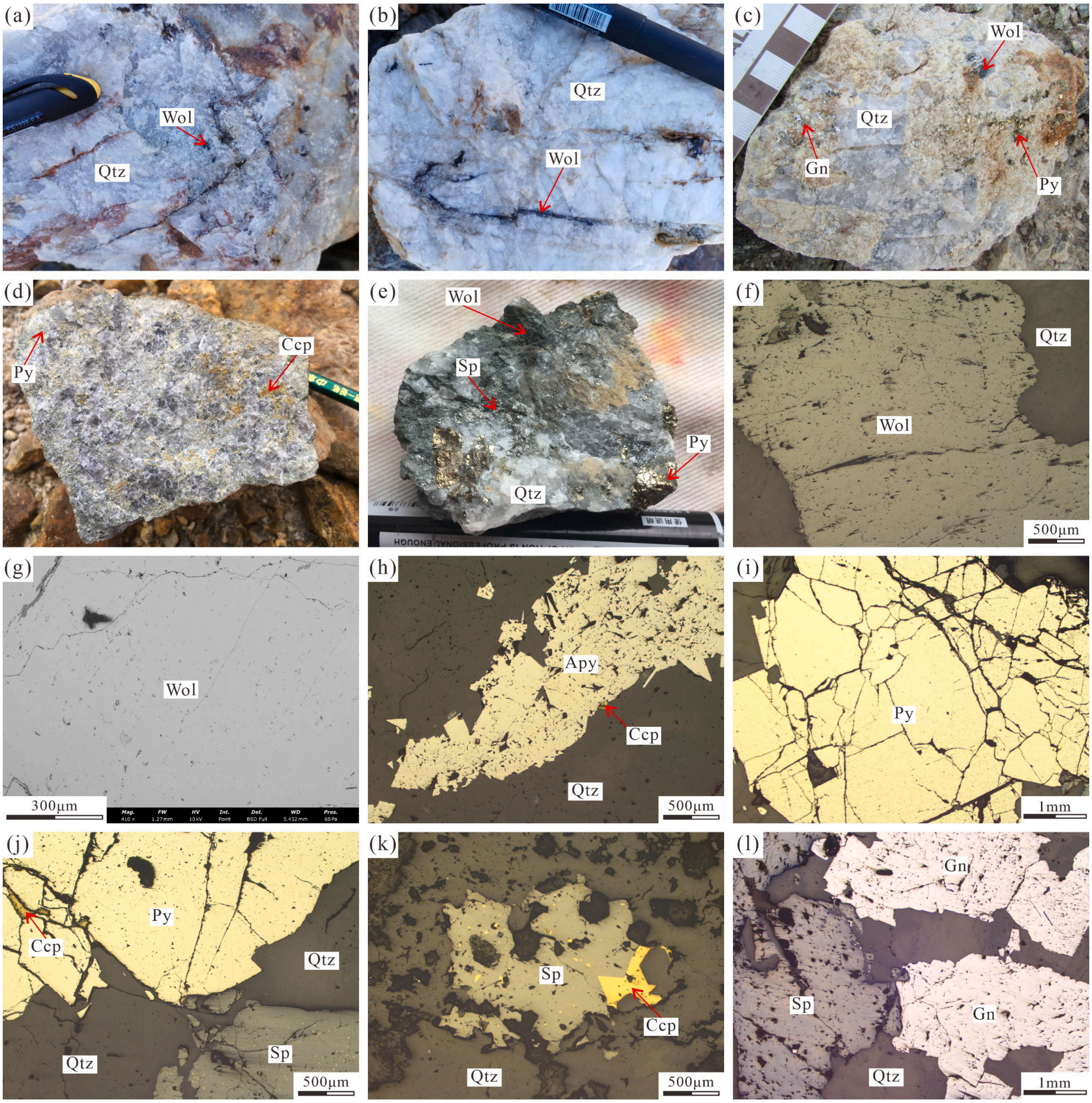

Fig. 5. Photographs (a–e), BSE images (g), and photomicrographs (f, h–l) of the Tantoushan ores. (a) The wolframite-bearing quartz ore. (b) Veins of wolframite in quartz. (c) The wolframite-pyrite-galena-quartz ore. (d) The chalcopyrite bearing quartz-pyrite ore; (e) The wolframite-pyrite-sphalerite-quartz ore. (f) Coarse-grained wolframite is intergrown with quartz. (g) Homogeneous wolframite without significant alteration. (h) arsenopyrite with rhomboid euhedral crystals, and replaced by chalcopyrite. (i) Crushed pyrite particles subjected to late stress. (j) Pyrite replaced by chalcopyrite, and sphalerite replacing pyrite along the margin. (k) Exsolution texture of sphalerite-chalcopyrite solid solution. Sphalerite replaced by chalcopyrite along the margin. (l) Galena intergrown with sphalerite, and the contact boundary between galena and sphalerite is smooth. Abbreviations: Qtz: quartz; Wol: wolframite; Py: pyrite; Gn: galena; Ccp: chalcopyrite; Sp: sphalerite; Apy: arsenopyrite.

arsenopyrite. Stage III is the final stage of the hydrothermal activity in the Tantoushan deposit. The veins of this stage are mainly composed of quartz, carbonate, and fluorite (Fig. 4h–j).

Different types of alteration are developed in the Tantoushan deposit, including silicification, K-feldspathization, sericitization, epidotization, fluoritization, and carbonatization (Fig. 4g–l). The W mineralization is spatially and genetically associated with silicification, K-feldspathization, and sericitization.

4. Sampling and analytical methods

4.1. Samples

Nine W-bearing granitic samples were collected from the open pit, and the sampling locations are indicated in Fig. 3. All granitic samples were prepared as thin sections for microscopic observation of mineral assemblages. Then, one granitic sample (TTS-9) was used for zircon U-Pb dating and *in situ* zircon Hf isotope analysis. Seven granitic samples

(TTS-10-3, TTS-10-4, TTS-10-5, TTS-10-6, TTS-10-7, TTS-11-1, and TTS-11-2) were used for the whole-rock major and trace element analyses. We collected ten wolframite ore samples from the open pit and an exploratory trench in the ore district, the locations of which are indicated in Fig. 3. The samples were prepared into polished probe sections for microscopic observations of mineral assemblages. Five wolframite samples were used for *in situ* U-Pb dating and major and trace element analyses. To better identify the internal wolframite textures and improve the reliability of the analytical data, BSE images of wolframite were generated at the Key Laboratory of Mineral Resources, Institute of Geology and Geophysics, Chinese Academy of Sciences (IGGCAS), Beijing, China. Wolframite crystals free of internal zoning, micro-inclusions, replacement phases, exsolution evidence, and alteration features were selected for *in situ* geochemical analyses.

4.2. Zircon U-Pb dating

U-Pb dating of zircon grains from the representative W-bearing monzogranite sample TTS-9 from the Tantoushan W deposit was performed using laser ablation-inductively coupled plasma-mass spectrometry (LA-ICP-MS). The selection of zircon grains was carried out at the mineral separation laboratory at the Regional Geology Minerals Investigation Research Institute, Hebei Province, China, using conventional density and magnetic separation techniques coupled with hand-picking under a binocular microscope. Transmitted and reflected microscopy images of the zircons were collected to examine the exterior structures. In addition, cathodoluminescence (CL) images were collected to examine the internal texture of the zircon grains in order to identify and select points suitable for U-Pb analyses.

The selected zircon grains were subjected to LA-ICP-MS analysis at the IGGCAS, Beijing. The operating conditions and detailed analytical methodology used were similar to those reported by Liu et al. (2010a). The analyses were conducted using an Agilent 7700e ICP-MS instrument coupled with a GeoLasPro laser. The laser spot size and frequency were 32 μm and 6 Hz, respectively. Zircon 91,500 was used as an external standard and was analyzed twice after every five-sample analyses. ICPMSDataCal software was used for quantitative calibration of trace element analyses and U-Pb dating (Liu et al., 2010a). The ISOPLOT software was used for age calculations and constructions of Concordia diagrams (Ludwig, 2003). The analytical data and Concordia plots were reported at 1σ errors, while the weighted mean ages were reported at confidence levels >95 %.

4.3. Wolframite in situ U-Pb dating

The wolframite sample TTS-7-1 was selected for laser ablation-sector field-inductively coupled plasma-mass spectrometry (LA-SF-ICP-MS) U-Pb analysis. The sample was ablated using a GeoLasPro 193 nm ArF excimer laser (CompexPro 102F, Coherent) coupled with a Thermo Scientific Element XR SF-ICP-MS at the State Key Laboratory of Ore Deposit Geochemistry, Institute of Geochemistry, Chinese Academy of Sciences, Guiyang, China. A detailed description of the analytical conditions and methods can be found in Tang et al. (2020, 2021). The ICP-MS data were processed offline using ICPMSDataCal software for calibrations, background corrections, and floating of the integration signal (Liu et al., 2010b). No downhole corrections were made for only the first ~25 s of ablation data (excluding the initial ~2 s) used in the whole process. Isoplot 4.15 was used to calculate the U-Pb ages and generate Concordia diagrams. Common Pb corrections were employed using a Tera-Wasserburg Concordia or a Tera-Wasserburg Concordia anchored through common Pb (Chew et al., 2011). Lower intercept ages were used as the timing of mineral precipitation of wolframite (Chew et al., 2011; Roberts et al., 2017; Luo et al., 2019). The data uncertainties for the isotopic ratios in the studied samples were reported at 1 σ.

4.4. In situ zircon Hf isotope analyses

In situ zircon Hf isotope analyses were conducted at the IGGCAS using a Thermo Scientific Neptune (Plus) multiple-collector-inductively coupled plasma-mass spectrometry (MC-ICP-MS) coupled to a New Wave 213 nm solid-state laser ablation system. The laser ablation beam had a diameter of 44 μm, laser repetition rate of 10 Hz, and laser energy of 10–11 J/cm^2. The ablated material was injected into the MC-ICP-MS with a high-purity He carrier gas. Details of the instrumental conditions and data acquisition protocols have been reported previously (Wu et al., 2006). The $^{176}Hf/^{177}Hf$ ratio was normalized to $^{179}Hf/^{177}Hf = 0.7325$. Hafnium isotopic data were age-corrected using a ^{176}Lu decay constant of 1.867×10^{-11} a^{-1} (Söderlund et al., 2004). The $\varepsilon_{Hf}(t)$ values and Hf model ages were calculated using methods reported by Bouvier et al. (2008) and Griffin et al. (2002), respectively.

4.5. Major and trace element analyses of monzogranites

The weathered surfaces of the monzogranite specimens were removed and the fresh parts were grounded in an agate mill to a 200-mesh size. The concentrations of the major and trace elements were determined at the ALS Chemex Center, Guangzhou, China. Major element analyses were performed using X-ray fluorescence (XRF) on a PANalytical PW2424 instrument (ME-XRF26d analytical package). Approximately 0.5 g of crushed whole-rock powder was dissolved in fusion with $LiNO_3$ to produce a glass bead for analysis. According to the measured values of the GSR-1 standard, the uncertainties were <5 %. Trace element concentrations were determined using a PerkinElmer Elan 9000 ICP-MS instrument (ME-MS81 analytical package). Approximately 50 mg of crushed whole-rock powder was dissolved in a $LiBO_2/Li_2B_4O_7$ mixture at ~1025 °C. The solution was then extracted after cooling and diluted with HF, HCl, and HNO_3 before the measurement. External standards BHVO-1 and G-2 were used to monitor the drift in the mass response during measurements. The precision was generally >10 % for most trace elements.

4.6. Electron probe microanalysis of wolframite

Electron probe microanalysis (EPMA) of the wolframite samples (TTS-2-1, TTS-4-1, and TTS-7-2) was carried out at the Wuhan Sample Solution Analytical Technology Co., Ltd., Wuhan, China. The major and minor elemental compositions of wolframite grains were determined using a JEOL JXA 8230 EPMA equipped with five wavelength dispersive X-ray spectrometers. For major element (W, Fe, Mn) analysis, an acceleration voltage of 15 kV, a beam current of 50 nA, and a beam diameter of 1 μm were used. Standards included wolframite [W], hematite [Fe], manganite [Mn], and Nb metal [Nb]. The spectral lines, peak times, and off-peak background times used for the WDS analyses were W (Lα, 10, 5), Fe (Kα, 10, 5), Mn (Kα, 10, 5), and Nb (Lα, 10, 5). The analytical uncertainties were 0.4 wt% for WO_3, 0.2 wt% for FeO, 0.1 wt % for MnO, and 0.05 wt% for Nb_2O_5. The detection limits for all the analyzed elements were below 0.01 wt%.

4.7. LA-ICP-MS analyses of wolframite

LA-ICP-MS analyses of the wolframite samples (TTS-4-2 and TTS-7-1) were performed at the Wuhan Sample Solution Analytical Technology Co., Ltd., Wuhan, China. Laser sampling was performed using a GeoLas2005 laser ablation system coupled with an Agilent7700e ICP-MS. The instrument settings and operation procedures used herein were similar to those described in detail by Xiong et al. (2017) and Liu et al. (2008). The time-resolved signal included two intervals: the background (20–30 s) and analytic signal (50 s). United States Geological Survey (USGS) reference glasses (BCR-2G, BIR-1G, and BHVO-2G) were used as the calibration standards. No internal standards were used, but multiple external standards (Liu et al., 2008) were applied to calculate element concentrations. The elemental concentrations of the USGS glasses can be found in the GeoReM database (http://georem.mpch-mainz.gwdg.de/). ICPMSDataCal software (Liu et al., 2008, 2010b) was used for offline data processing, including analytical and background signal determinations, sensitivity drift calibrations, and element concentration calculations.

5. Results

5.1. Zircon U-Pb age

The zircon U-Pb isotope dating results for the monzogranite sample TTS-9 are listed in Table 1. The selected zircon grains for analysis are transparent, colourless, euhedral, and prismatic with lengths of 89–180 μm and length-to-width ratios of 1:1 to 2.5:1. CL images revealed typical igneous oscillatory zoning without a core-rim structure in the zircons (Fig. 6a). All zircons have high Th/U ratios (0.40–0.67), which are indicative of a magmatic origin (Belousova et al., 2002). Sixteen out of 18 spot analyses yielded a narrow and concordant age grouping, with a weighted mean $^{206}Pb/^{238}U$ age of 233.1 ± 1.8 Ma (1σ, MSWD = 0.41), representing the crystallization age of the W-bearing monzogranite (Fig. 6b). The two outliers have $^{206}Pb/^{238}U$ ages of 247.4 Ma (TTS-9-09) and 223.9 Ma (TTS-9-14), respectively.

5.2. Wolframite U-Pb age

The U-Pb isotope data for wolframite sample TTS-7-1 are listed in Table 2. The uncorrected U-Pb data are plotted using the U-Pb Tera-Wasserburg diagrams (Fig. 6c). Twenty-four spot analyses show total Pb, Th, and U concentrations of 0.23–20.02, 0.09–1.87, and 4.64–33.41 ppm, respectively. A lower intercept $^{206}Pb/^{238}U$ age of 234.3 ± 6.2 Ma (1σ, MSWD = 0.41) was obtained in the Tera-Wasserburg Concordia diagram (Fig. 6c).

5.3. In situ zircon Hf isotopes

The zircon Hf isotope data for monzogranite sample TTS-9 are listed in Table 3. The results show that the zircon grains have relatively consistent Hf isotopic compositions, with initial $^{176}Hf/^{177}Hf$ ratios ranging from 0.282135 to 0.282388, $\varepsilon_{Hf}(t)$ values from −17.7 to −8.6, and two-stage model ages (T_{DM2}) from 1807 to 2378 Ma. The $\varepsilon_{Hf}(t)$ versus age diagram (Fig. 7) reveals that all analyzed zircon spots from the monzogranite are plotted below the chondritic uniform reservoir line.

5.4. Whole-rock major and trace elements of monzogranites

The whole-rock geochemical data are presented in Table 4. The monzogranite contains 75.09–78.13 wt% SiO_2, 0.38–0.77 wt% CaO, 0.01–0.02 wt% P_2O_5, 10.59–12.80 wt% Al_2O_3, 0.04–0.12 wt% TiO_2, 0.95–1.85 wt% $Fe_2O_3^T$, 0.02–0.04 wt% MnO, and 7.45–8.63 wt% $K_2O + Na_2O$. Additionally, these samples contain 0.03–0.12 wt% MgO and had $Mg^{\#}$ values of 4.50–11.96. As shown in the total alkali versus SiO_2 diagram (Middlemost, 1994), most monzogranite samples are plotted in the granite field (Fig. 8a). In the K_2O versus SiO_2 diagram (Peccerillo and Taylor, 1976), the samples are mainly plotted in the high-K calc-alkaline

Table 1
Zircon LA-ICP-MS U-Pb dating data for sample TTS-9 from the Tantoushan W deposit.

Sample no.	Th	U	Pb	Th/U	$^{207}Pb/^{206}Pb$		$^{207}Pb/^{235}U$		$^{206}Pb/^{238}U$		$^{207}Pb/^{206}Pb$		$^{207}Pb/^{235}U$		$^{206}Pb/^{238}U$	
	(ppm)	(ppm)	(ppm)		Ratio	1σ	Ratio	1σ	Ratio	1σ	Ages (Ma)	1σ	Ages (Ma)	1σ	Ages (Ma)	1σ
TTS-9-01	242.9	459.7	24.1	0.53	0.05171	0.00222	0.26204	0.01110	0.03667	0.00053	272.3	98.1	236.3	8.9	232.2	3.3
TTS-9-02	130.0	247.9	13.1	0.52	0.05469	0.00349	0.27236	0.01452	0.03662	0.00075	398.2	175.0	244.6	11.6	231.9	4.7
TTS-9-03	166.5	315.5	16.8	0.53	0.05288	0.00333	0.26079	0.01383	0.03644	0.00065	324.1	144.4	235.3	11.1	230.7	4.1
TTS-9-04	163.0	304.0	16.5	0.54	0.05131	0.00302	0.25740	0.01439	0.03654	0.00057	253.8	130.5	232.6	11.6	231.4	3.6
TTS-9-05	279.0	527.9	30.2	0.53	0.05265	0.00237	0.26644	0.01122	0.03669	0.00059	322.3	101.8	239.8	9.0	232.3	3.7
TTS-9-06	222.0	398.0	22.8	0.56	0.05156	0.00238	0.25816	0.01115	0.03647	0.00062	264.9	100.9	233.2	9.0	230.9	3.8
TTS-9-07	150.7	261.9	14.7	0.58	0.05430	0.00321	0.27116	0.01525	0.03669	0.00074	383.4	126.8	243.6	12.2	232.3	4.6
TTS-9-08	221.7	466.4	24.6	0.48	0.05474	0.00270	0.28148	0.01294	0.03756	0.00058	466.7	111.1	251.8	10.3	237.7	3.6
TTS-9-09	337.8	794.9	38.4	0.42	0.05392	0.00173	0.29127	0.00867	0.03913	0.00056	368.6	72.2	259.6	6.8	247.4	3.5
TTS-9-10	177.9	281.3	16.0	0.63	0.05084	0.00260	0.25763	0.01296	0.03644	0.00066	235.3	118.5	232.8	10.5	230.7	4.1
TTS-9-11	481.5	713.9	43.7	0.67	0.05430	0.00184	0.28168	0.00958	0.03742	0.00047	383.4	75.9	252.0	7.6	236.8	2.9
TTS-9-12	236.9	543.4	27.1	0.44	0.05545	0.00222	0.27877	0.01064	0.03657	0.00056	431.5	88.9	249.7	8.4	231.5	3.5
TTS-9-13	121.4	219.9	11.4	0.55	0.05483	0.00430	0.26759	0.01915	0.03627	0.00085	405.6	175.9	240.8	15.3	229.7	5.3
TTS-9-14	444.5	776.0	43.0	0.57	0.05634	0.00210	0.27583	0.01030	0.03534	0.00048	464.9	78.7	247.3	8.2	223.9	3.0
TTS-9-15	355.4	880.6	38.5	0.40	0.04958	0.00161	0.25349	0.00836	0.03680	0.00053	176.0	75.9	229.4	6.8	233.0	3.3
TTS-9-16	280.9	551.4	28.0	0.51	0.05014	0.00221	0.25622	0.01127	0.03688	0.00055	211.2	103.7	231.6	9.1	233.5	3.4
TTS-9-17	142.8	255.3	13.3	0.56	0.05393	0.00295	0.27041	0.01429	0.03665	0.00068	368.6	124.1	243.0	11.4	232.0	4.2
TTS-9-18	262.9	609.3	31.7	0.43	0.05563	0.00209	0.28618	0.01007	0.03727	0.00051	438.9	83.3	255.5	8.0	235.9	3.2

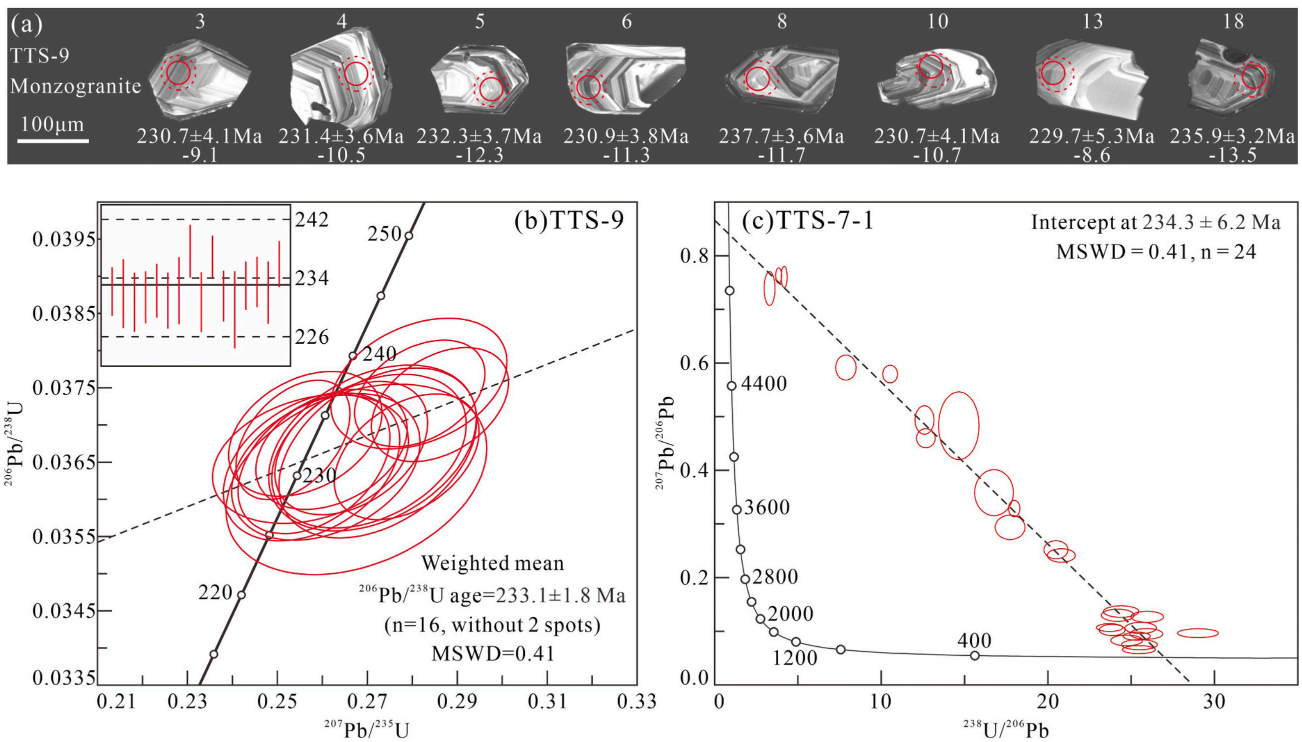

Fig. 6. (a) Cathodoluminescence images of zircons separated from monzogranite sample TTS-9. Red solid circles are the locations of U-Pb analyses and dashed circles are the locations of Hf analyses. (b) Zircon U-Pb Concordia diagrams for the monzogranite from the Tantoushan deposit. (c) Tera-Wasserburg plots and the lower intercepts ages of wolframite samples TTS-7-1 from the Tantoushan deposit. (For interpretation of the references to colour in this figure legend, the reader is referred to the web version of this article.)

Table 2
LA-SF-ICP-MS U-Pb isotope data of the wolframite sample TTS-7-1 from the Tantoushan W deposit.

Sample	Pb	Th	U	$^{207}Pb/^{206}Pb$		$^{207}Pb/^{235}U$		$^{206}Pb/^{238}U$		Rho	$^{238}U/^{206}Pb$		$^{207}Pb/^{206}Pb$	
	ppm			Ratio	1sigma	Ratio	1sigma	Ratio	1sigma		Ratio	Percent	Ratio	Percent
TTS-7-1-01	4.30	0.17	4.64	0.73854	0.02073	27.53913	7.09410	0.26325	0.01717	0.25327	3.305	6.524	0.739	2.807
TTS-7-1-02	20.02	1.67	25.38	0.76286	0.00939	23.96070	5.98550	0.22634	0.00706	0.12481	3.844	3.118	0.763	1.231
TTS-7-1-03	13.45	1.08	19.35	0.76011	0.01308	21.87500	5.45881	0.20829	0.00585	0.11255	4.177	2.809	0.760	1.720
TTS-7-1-04	3.59	0.66	11.77	0.59142	0.01538	9.34305	2.38373	0.11035	0.00568	0.20159	7.884	5.143	0.591	2.601
TTS-7-1-05	3.79	1.87	15.70	0.57924	0.01089	6.58442	1.64377	0.08254	0.00230	0.11154	10.541	2.785	0.579	1.881
TTS-7-1-06	1.10	0.36	6.18	0.49346	0.01754	4.52635	1.13135	0.06905	0.00208	0.12031	12.600	3.007	0.493	3.555
TTS-7-1-07	2.00	0.51	11.98	0.45976	0.01167	4.36061	1.09213	0.06860	0.00201	0.11693	12.681	2.929	0.460	2.538
TTS-7-1-08	0.97	0.23	6.17	0.35818	0.02833	2.87517	0.76385	0.05188	0.00238	0.17282	16.771	4.591	0.358	7.910
TTS-7-1-09	1.17	0.21	13.38	0.29362	0.01515	2.00455	0.50921	0.04905	0.00164	0.13144	17.738	3.339	0.294	5.159
TTS-7-1-10	3.21	0.44	33.41	0.32873	0.01007	2.18600	0.54521	0.04836	0.00060	0.04998	17.988	1.246	0.329	3.062
TTS-7-1-11	0.78	0.49	10.51	0.25179	0.01115	1.40139	0.34991	0.04245	0.00099	0.09298	20.493	2.322	0.252	4.428
TTS-7-1-12	0.92	0.49	13.48	0.24124	0.00829	1.37098	0.34375	0.04180	0.00112	0.10651	20.814	2.670	0.241	3.437
TTS-7-1-13	0.39	0.13	7.43	0.08459	0.00654	0.41960	0.10822	0.03791	0.00117	0.11984	22.948	3.091	0.085	7.732
TTS-7-1-14	0.79	0.38	16.89	0.10672	0.00472	0.52810	0.13264	0.03669	0.00081	0.08829	23.710	2.218	0.107	4.426
TTS-7-1-15	0.23	0.09	4.95	0.08123	0.00870	0.35930	0.09527	0.03669	0.00137	0.14097	23.710	3.738	0.081	10.705
TTS-7-1-16	0.59	0.23	12.13	0.10223	0.00687	0.50009	0.12743	0.03645	0.00078	0.08435	23.865	2.149	0.102	6.725
TTS-7-1-17	0.52	0.24	10.33	0.12991	0.00751	0.64716	0.16514	0.03596	0.00097	0.10588	24.197	2.702	0.130	5.781
TTS-7-1-18	0.53	0.22	10.24	0.13674	0.00710	0.65785	0.16707	0.03565	0.00103	0.11398	24.407	2.895	0.137	5.190
TTS-7-1-19	0.58	0.31	13.01	0.08281	0.00653	0.37133	0.09504	0.03517	0.00090	0.09961	24.738	2.550	0.083	7.890
TTS-7-1-20	0.91	0.36	21.32	0.09076	0.00496	0.41112	0.10334	0.03433	0.00073	0.08508	25.339	2.139	0.091	5.465
TTS-7-1-21	0.57	0.24	13.63	0.06577	0.00491	0.30035	0.07741	0.03416	0.00088	0.09977	25.466	2.571	0.066	7.463
TTS-7-1-22	0.37	0.12	8.03	0.07479	0.00624	0.34887	0.09119	0.03412	0.00095	0.10672	25.495	2.790	0.075	8.345
TTS-7-1-23	0.52	0.23	11.71	0.10600	0.00685	0.48185	0.12250	0.03401	0.00083	0.09647	25.580	2.453	0.106	6.460
TTS-7-1-24	0.58	0.20	13.60	0.09498	0.00650	0.42522	0.10879	0.03356	0.00084	0.09824	25.921	2.513	0.095	6.846

field (Fig. 8b). On an A/NK (molar $Al_2O_3/(Na_2O + K_2O)$) versus A/CNK (molar $Al_2O_3/(CaO + Na_2O + K_2O)$) diagram (Maniar and Piccoli, 1989), they are plotted as metaluminous to weakly peraluminous rocks (Fig. 8c). The monzogranite show 'seagull' forms in chondrite-normalized rare earth elements (REEs) diagrams (Fig. 9a), containing total REE concentrations of 61.65–208.05 ppm, light REEs (LREEs)/ heavy REE (HREE) ratios of 3.18–13.49, $(La/Yb)_N$ of 1.94–15.95, and δEu of 0.05–0.29, revealing weak REE fractionation and a strongly negative Eu anomaly. These characteristics are different from those of Triassic W-barren granitoids in NE China, but similar to those of highly fractionated granites (Miller and Mittlefehldt, 1982, 1984). In the primitive-mantle-normalized trace element diagram (Sun and McDonough, 1989), all monzogranite samples show enrichment in Rb, Th, U, K, and Pb (Fig. 9b). Compared to the Triassic W-barren granitoids, the

Table 3
Hf isotopic compositions of zircons from sample TTS-9 in the Tantoushan W deposit.

Sample no.	$^{176}Hf/^{177}Hf$	2σ	$^{176}Lu/^{177}Hf$	2σ	$^{176}Yb/^{177}Hf$	2σ	Age (Ma)	$\varepsilon_{Hf}(0)$	$\varepsilon_{Hf}(t)$	T_{DM1}	T_{DM2}	$f_{Lu/Hf}$
TTS-9-01	0.282343	0.000022	0.000762	0.000016	0.025748	0.0004	232.2	−15.2	−10.2	1276	1908	−0.98
TTS-9-02	0.282369	0.000026	0.000627	0.000002	0.020226	0.0001	231.9	−14.3	−9.3	1235	1849	−0.98
TTS-9-03	0.282375	0.000023	0.000584	0.000001	0.019007	0.0002	230.7	−14.0	−9.1	1225	1835	−0.98
TTS-9-04	0.282335	0.000020	0.000705	0.000007	0.022357	0.0001	231.4	−15.5	−10.5	1285	1926	−0.98
TTS-9-05	0.282284	0.000021	0.000746	0.000006	0.022079	0.0001	232.3	−17.3	−12.3	1357	2039	−0.98
TTS-9-06	0.282314	0.000020	0.000803	0.000001	0.026400	0.0002	230.9	−16.2	−11.3	1317	1974	−0.98
TTS-9-07	0.282364	0.000018	0.000546	0.000013	0.016722	0.0004	232.3	−14.4	−9.4	1239	1858	−0.98
TTS-9-08	0.282297	0.000018	0.000805	0.000003	0.025534	0.0001	237.7	−16.8	−11.7	1341	2008	−0.98
TTS-9-09	0.282359	0.000018	0.000786	0.000012	0.023665	0.0005	247.4	−14.6	−9.3	1255	1864	−0.98
TTS-9-10	0.282330	0.000022	0.000675	0.000004	0.022703	0.0002	230.7	−15.6	−10.7	1290	1936	−0.98
TTS-9-11	0.282264	0.000025	0.001100	0.000012	0.032549	0.0003	236.8	−18.0	−12.9	1397	2084	−0.97
TTS-9-12	0.282135	0.000045	0.001526	0.000052	0.044943	0.0015	231.5	−22.5	−17.7	1596	2378	−0.95
TTS-9-13	0.282388	0.000024	0.000542	0.000007	0.018250	0.0003	229.7	−13.6	−8.6	1206	1807	−0.98
TTS-9-14	0.282325	0.000026	0.000806	0.000011	0.024110	0.0003	223.9	−15.8	−11.0	1303	1954	−0.98
TTS-9-15	0.282312	0.000019	0.001054	0.000011	0.030816	0.0002	233.0	−16.3	−11.3	1328	1978	−0.97
TTS-9-16	0.282362	0.000022	0.000822	0.000007	0.025923	0.0004	233.5	−14.5	−9.5	1251	1865	−0.98
TTS-9-17	0.282369	0.000027	0.000809	0.000013	0.024562	0.0002	232.0	−14.2	−9.3	1240	1849	−0.98
TTS-9-18	0.282247	0.000027	0.000940	0.000021	0.027504	0.0007	235.9	−18.6	−13.5	1415	2121	−0.97

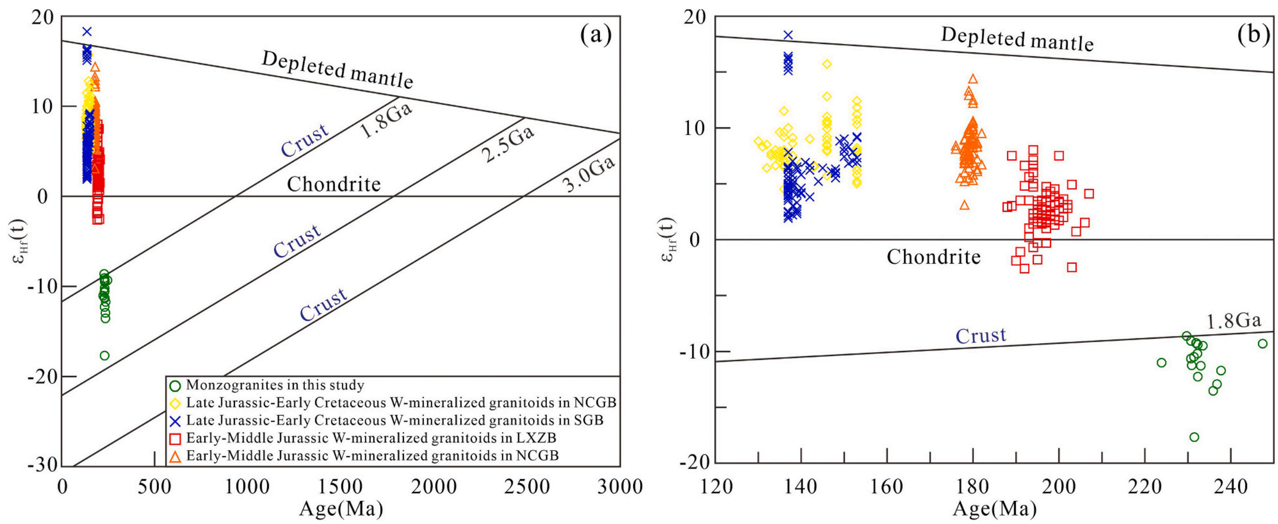

Fig. 7. $\varepsilon_{Hf}(t)$ versus age (t) diagrams for the monzogranite from the Tantoushan W deposit and Mesozoic W-mineralized granitoids in NE China. Data for the Mesozoic W-mineralized granitoids in NE China are listed in Table S3.

samples exhibit stronger negative Ba, Sr, P, and Ti anomalies (Fig. 9b).

5.5. In situ major and trace element compositions of wolframite

The chemical compositions of wolframite from the Tantoushan W deposit determined using EPMA are listed in Table S1. The wolframite trace element concentrations measured using LA-ICP-MS are listed in Table S2.

The wolframite samples contain 75.30–76.98 wt% WO_3, 8.59–15.80 wt% FeO, 7.69–14.89 wt% MnO, and 0.03–0.42 wt% Nb_2O_5 (Table S1). They have relatively uniform Mn/(Mn + Fe) ratios of 0.33–0.64 (Fig. 10a). The wolframite samples are characterized by variable trace element compositions. Five elements with contents near or above 10 ppm were detected, namely Sc of 5.79–25.75 ppm (average 14.35 ppm), Zn of 21.91–138.75 ppm (average 56.08 ppm), Y of 4.33–44.39 ppm (average 15.99 ppm), Zr of 8.91–30.40 ppm (average 15.27 ppm), and Nb of 26.69–1832.34 ppm (average 240.04 ppm). The V, Cr, Ni, Sn, Dy, Er, Yb, Ta, and U contents are <10 ppm, and the rest of trace elements are <1 ppm in content (Table S2). The total REE concentrations of wolframite range from 4.79 to 36.96 ppm. All samples have very low LREE concentrations (0.04–1.23 ppm) and relatively high HREE concentrations (4.75–36.18 ppm). All REE patterns for the wolframite sample normalized to the upper continental crust (UCC from Rudnick and Gao, 2003) display similar signatures with a common preferential enrichment in HREEs relative to LREEs (Fig. 11a). In the UCC-normalized trace element diagram, all the wolframite samples display similar trace element signatures with relative enrichments in U, Nb, Ta, Sc, Sn, and Zn, and relative depletions in Rb, Ba, K, Sr, Hf, and Ti (Fig. 11b).

6. Discussion

6.1. Timing of granitic magmatism and W mineralization

Constraints on the timing and duration of magmatic-hydrothermal events are crucial for understanding ore deposit formation from both academic and economic viewpoints (Stein, 2014). Accurate isotopic dating of hydrothermal minerals is a vital tool for determining the timing of hydrothermal activity relative to intrusive magmatism, which is critical for constructing genetic models of hydrothermal deposits (Li et al., 2021b). Wolframite collected from hydrothermal quartz veins in quartz vein-type W deposits can represent the main product of hydrothermal activity and is therefore proposed as a U-Pb geochronometer for direct dating of W mineralization events (Carr et al., 2021). In recent years, wolframite *in situ* U-Pb geochronology has been successfully applied to constrain the absolute timing and duration of W-forming

Table 4
Major (wt%) and trace element (ppm) compositions of monzogranites from the Tantoushan W deposit.

Sample	TTS-10-3	TTS-10-4	TTS-10-5	TTS-10-6	TTS-10-7	TTS-11-1	TTS-11-2
Lithology	Monzogranite	Monzogranite	Monzogranite	Monzogranite	Monzogranite	Monzogranite	Monzogranite
SiO_2	75.72	75.49	75.09	76.45	78.13	76.94	77.37
Al_2O_3	12.60	12.80	12.71	12.06	10.59	12.62	12.38
$Fe_2O_3^T$	1.75	1.26	1.76	1.84	1.85	0.95	1.10
FeO^T	1.57	1.13	1.58	1.66	1.66	0.85	0.99
CaO	0.77	0.60	0.67	0.57	0.64	0.38	0.40
MgO	0.12	0.03	0.10	0.11	0.07	0.03	0.03
K_2O	4.30	4.67	5.02	4.31	4.65	4.53	4.45
Na_2O	3.73	3.96	3.58	3.56	2.80	3.87	3.77
TiO_2	0.12	0.05	0.11	0.12	0.09	0.04	0.04
MnO	0.03	0.02	0.04	0.04	0.04	0.02	0.03
P_2O_5	0.02	0.01	0.02	0.02	0.01	0.01	0.01
Mg#	11.96	4.50	10.12	10.59	6.97	5.89	5.13
σ	1.97	2.29	2.30	1.85	1.58	2.08	1.97
A/NK	1.17	1.11	1.12	1.15	1.10	1.12	1.12
A/CNK	1.03	1.01	1.01	1.04	0.98	1.06	1.05
Na_2O/K_2O	0.87	0.85	0.71	0.83	0.60	0.85	0.85
$Na_2O + K_2O$	8.03	8.63	8.60	7.87	7.45	8.40	8.22
LOI	0.58	0.60	0.54	0.41	0.53	0.76	0.65
La	47.60	17.30	46.90	46.20	37.10	10.30	15.30
Ce	90.60	37.20	95.40	91.40	80.50	25.20	37.80
Pr	9.43	4.31	10.00	9.94	8.99	2.53	4.20
Nd	27.60	15.90	30.40	30.60	29.20	8.00	13.80
Sm	4.92	4.36	6.28	6.21	7.43	2.20	3.73
Eu	0.40	0.12	0.30	0.27	0.15	0.09	0.06
Gd	3.74	4.89	4.82	4.72	7.61	2.21	3.81
Tb	0.61	0.99	0.85	0.81	1.48	0.47	0.81
Dy	3.37	6.08	4.76	4.53	9.41	3.22	5.51
Ho	0.72	1.38	1.02	0.96	2.13	0.79	1.41
Er	2.12	4.53	3.07	2.84	6.95	2.58	4.60
Tm	0.33	0.77	0.50	0.44	1.19	0.43	0.80
Yb	2.14	5.21	3.23	2.88	7.94	3.12	5.66
Lu	0.35	0.81	0.52	0.48	1.35	0.51	0.94
Y	26.30	56.20	39.20	33.00	94.50	33.60	56.70
Rb	314.00	381.00	388.00	369.00	430.00	386.00	424.00
Sr	59.50	15.50	43.10	41.20	21.20	8.60	8.20
Ba	163.00	32.60	181.50	112.00	67.50	28.00	22.30
U	3.82	5.45	4.31	3.95	12.35	9.28	7.21
Th	47.50	52.70	56.00	45.30	56.40	29.60	30.80
Nb	21.40	44.70	35.30	33.10	41.20	38.00	38.90
Ta	2.16	4.20	3.64	3.47	5.13	3.82	4.88
Zr	177.00	138.00	185.00	167.00	233.00	123.00	149.00
Hf	5.30	5.70	6.20	5.30	9.30	5.70	7.10
Li	65.20	48.10	69.50	76.90	90.40	47.10	78.80
V	8.00	5.00	7.00	11.00	5.00	34.00	5.00
Cr	20.00	20.00	30.00	30.00	20.00	20.00	20.00
Co	1.20	0.40	1.10	1.10	0.70	0.40	0.30
Ni	1.00	1.00	1.10	1.30	1.40	1.30	1.10
Ga	25.20	25.80	26.00	25.50	23.70	25.30	26.50
Cs	8.17	10.30	11.40	12.20	21.40	8.14	11.75
Sc	0.60	0.40	0.80	0.80	0.70	0.70	0.70
Ag	0.01	0.01	0.01	0.01	0.01	0.01	0.01
Cu	0.20	0.20	0.20	0.20	0.20	0.20	0.20
Mo	1.43	1.64	1.46	1.48	2.04	1.08	1.29
Pb	36.80	52.40	41.70	40.20	44.40	48.00	44.80
Sn	6.00	10.00	8.00	10.00	16.00	8.00	13.00
Zn	45.00	30.00	52.00	61.00	59.00	26.00	37.00
W	11.20	12.60	10.00	9.60	8.60	10.60	8.00
∑REE	193.93	103.85	208.05	202.28	201.43	61.65	98.43
LREE/HREE	13.49	3.21	10.08	10.45	4.29	3.62	3.18
$(La/Yb)_N$	15.95	2.38	10.42	11.51	3.35	2.37	1.94
δEu	0.29	0.08	0.17	0.15	0.06	0.12	0.05
Sr/Y	2.26	0.28	1.10	1.25	0.22	0.26	0.14
Th/Yb	22.20	10.12	17.34	15.73	7.10	9.49	5.44
Ta/Yb	1.01	0.81	1.13	1.20	0.65	1.22	0.86
Ta/Nb	0.10	0.09	0.10	0.10	0.12	0.10	0.13
Nb/Yb	10.00	8.58	10.93	11.49	5.19	12.18	6.87
Lu/Yb	0.16	0.16	0.16	0.17	0.17	0.16	0.17
Rb/Sr	5.28	24.58	9.00	8.96	20.28	44.88	51.71
La/Sm	9.67	3.97	7.47	7.44	4.99	4.68	4.10
Zr/Hf	33.40	24.21	29.84	31.51	25.05	21.58	20.99
Ti/Zr	4.06	2.17	3.56	4.31	2.32	1.95	1.61
Ti/Y	27.35	5.33	16.82	21.80	5.71	7.14	4.23
Nb/Ta	9.91	10.64	9.70	9.54	8.03	9.95	7.97

(*continued on next page*)

Table 4 (*continued*)

Sample	TTS-10-3	TTS-10-4	TTS-10-5	TTS-10-6	TTS-10-7	TTS-11-1	TTS-11-2
Lithology	Monzogranite	Monzogranite	Monzogranite	Monzogranite	Monzogranite	Monzogranite	Monzogranite
Zr/Nb	8.27	3.09	5.24	5.05	5.66	3.24	3.83
Dy/Yb	1.57	1.17	1.47	1.57	1.19	1.03	0.97
La/Yb	22.24	3.32	14.52	16.04	4.67	3.30	2.70
U/Th	0.08	0.10	0.08	0.09	0.22	0.31	0.23
K/Rb	113.68	101.75	107.40	96.96	89.77	97.42	87.12
Y/Ho	36.53	40.72	38.43	34.38	44.37	42.53	40.21
R1	2665.38	2496.04	2508.53	2769.73	3072.42	2665.22	2744.27
R2	336.47	317.75	326.94	303.94	280.49	290.67	288.08
T_{Zr}(°C)	821	819	819	825	822	827	827

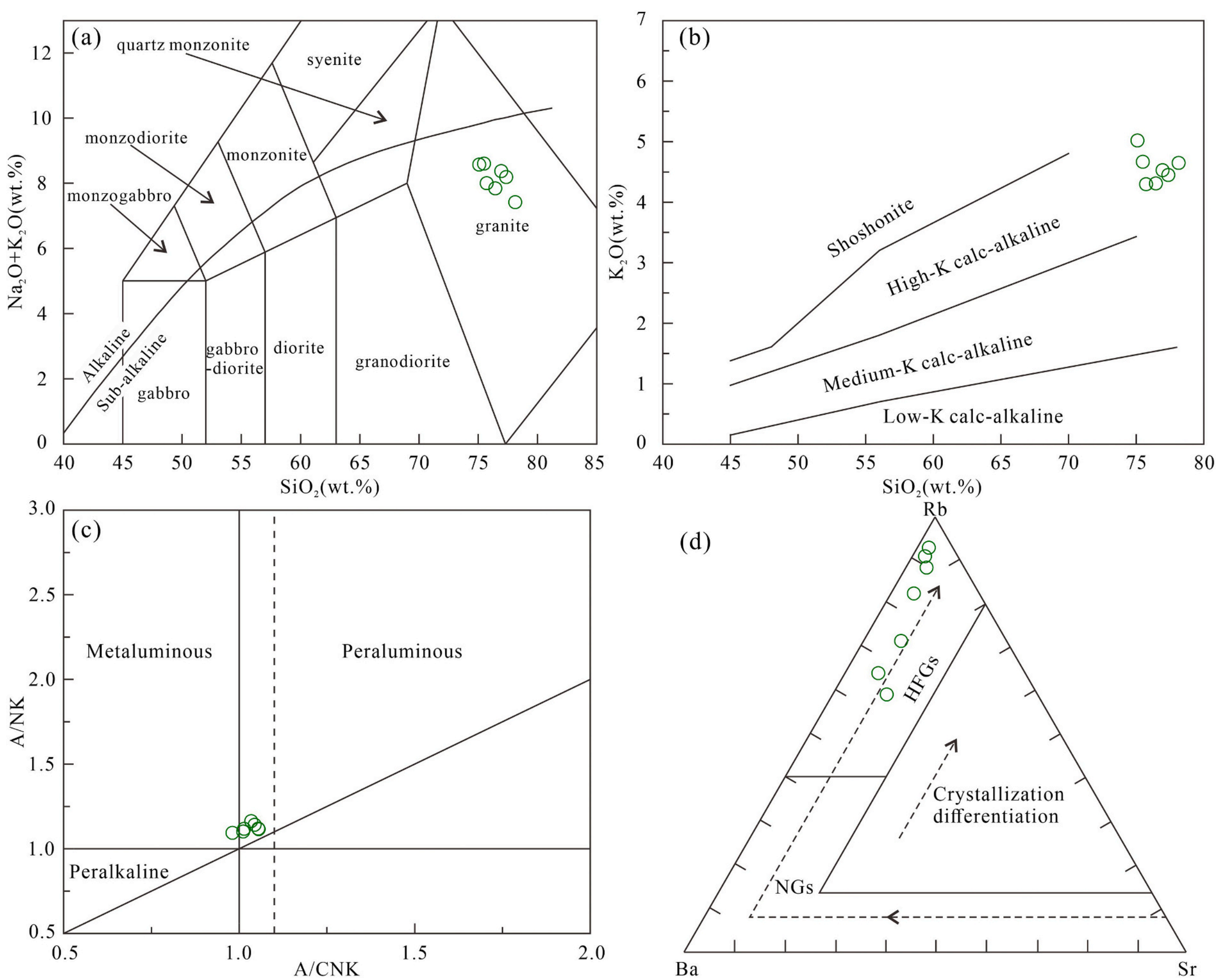

Fig. 8. (a) TAS (total alkali silica) diagram (after Middlemost, 1994). (b) K_2O versus SiO_2 diagram (after Peccerillo and Taylor, 1976). (c) A/NK versus A/CNK diagram (after Maniar and Piccoli, 1989). (d) Rb-Ba-Sr diagram (after El Bouseily and El Sokkary, 1975). Abbreviations are as follow: HFGs = highly fractionated granites; NGs = normal granites.

magmatic-hydrothermal systems (Deng et al., 2019; Tang et al., 2020; Yang et al., 2020; Li et al., 2021b; Yang et al., 2022).

In this study, *in situ* U-Pb dating of wolframite from the Tantoushan deposit yielded a lower intercept $^{206}Pb/^{238}U$ age of 234.3 ± 6.2 Ma (1σ, MSWD = 0.41) (Fig. 6c). The zircon U-Pb age of the W-bearing monzogranite indicates that the intrusion was emplaced at 233.1 ± 1.8 Ma (1σ, MSWD = 0.41) (Fig. 6b). The similarity of these ages indicates that the Late Triassic W mineralization in the Tantoushan deposit was synchronous with and genetically related to the W-bearing monzogranite, supporting a Late Triassic intrusive-related origin for the deposit.

By collecting published geochronological data of W deposits in NE China, Xie et al. (2021b) concluded that there are three periods of W mineralization events: Triassic (240–250 Ma), Early–Middle Jurassic (170–200 Ma), and Late Jurassic–Early Cretaceous (125–160 Ma). W-related granitic magmatism in NE China began in the Early Triassic and peaked in the Late Jurassic–Early Cretaceous (Xie et al., 2021b). Previous studies mainly focused on the Jurassic and Early Cretaceous granitic magmatism and associated W mineralization. In contrast, only a few studies focused on the Triassic deposits, limiting our understanding of regional tectonic-magmatic-hydrothermal events. To date, only two W deposits have been interpreted to be of Triassic age, including the Shazigou W-Mo deposit and Yangjingou W deposit. Peng et al. (2015) reported a molybdenite weighted mean Re-Os age (243.8 ± 1.6 Ma) from five molybdenite samples from the Shazigou W-Mo deposit. Zhao

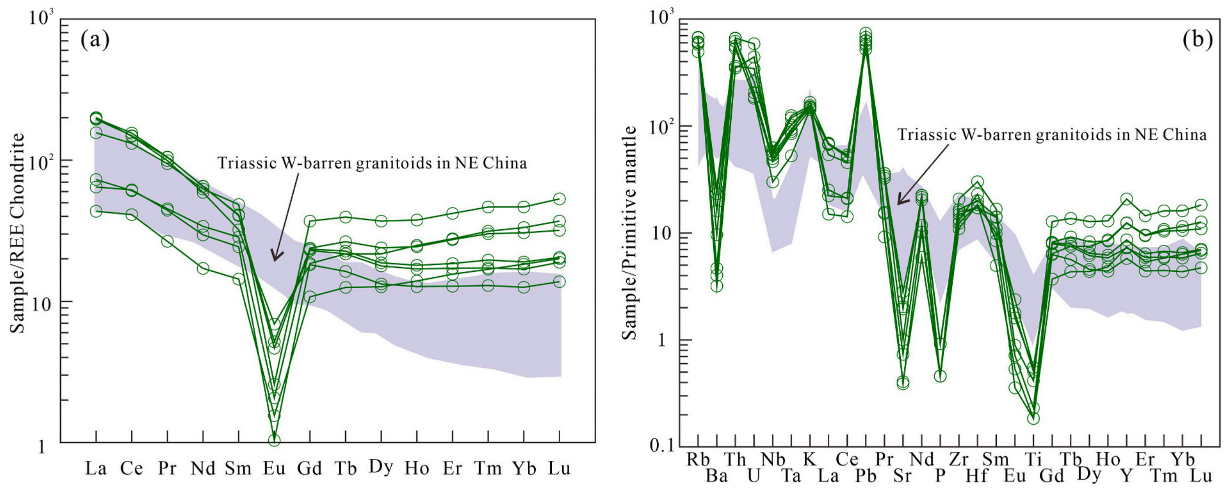

Fig. 9. (a) Chondrite-normalized REE patterns and (b) primitive-mantle-normalized trace element spider diagrams for the monzogranite from the Tantoushan W deposit (normalization values are from Sun and McDonough, 1989). Data of Triassic W-barren granitoids in NE China were shown in Table S4.

(2014) reported a zircon U-Pb age of 249.4 ± 2.7 Ma for the granodiorite and a muscovite ^{40}Ar-^{39}Ar age of 230.8 ± 1.2 Ma for the Yangjingou W deposit. It is noteworthy that the Shazigou W-Mo, Yangjingou W, and Tantoushan W deposits are all located along the SXCF, which may correspond to a tectonic setting of the closure of the PAO during the Triassic. These isotopic ages may elucidate the intensive and extensive Triassic tectonic-magmatic activities in the region. Therefore, not only the Jurassic and Early Cretaceous W mineralization pervasive in NE China but also the Triassic W mineralization events are prevalent during the Mesozoic. Discovery of Triassic W deposits in NE China, particularly along both sides of the SXCF, represents future prospecting potential.

6.2. Petrogenesis of the W-bearing monzogranites

Granitic rocks are generally divided into S-, I-, and A-types, mainly according to their protolith nature and associated tectonic setting (Whalen et al., 1987; Chappell, 1999). The Tantoushan monzogranites show petrological and geochemical characteristics of I-type granitoids (Chappell and White, 1992). These features include: (1) abundance of biotite (5–10 vol%) and absence of muscovite, cordierite, or mafic alkaline minerals, such as arfvedsonite and riebeckite; (2) metaluminous to weakly peraluminous composition with A/CNK ratios of 0.98–1.06 (Fig. 8c); (3) relatively low contents of Zr + Nb + Ce + Y (<350 ppm), $K_2O + Na_2O$ (7.45–8.63 wt%), Zr (123–233 ppm), Ce (25.20–95.40 ppm), Y (26.30–94.50 ppm), Zn (26–61 ppm), and low values of $(K_2O + Na_2O)/CaO$ (10.43–22.11) and 10,000 × Ga/Al (<2.6) (Fig. 12), which are not typical of A-type granites (Whalen et al., 1987); and (4) low concentrations of P_2O_5 (<0.10 wt%) that are similar to those of I-type granites and inconsistent with those of S-type granites (Chappell and White, 2001).

The Tantoushan monzogranites appear to have a common magmatic origin, with similar variation trends in major and trace elements and zircon Hf isotope compositions. Various models have been proposed for the origin of I-type granites, including: (a) fractional crystallization of mantle-derived magmas that underplate the lower crust (Manya and Maboko, 2016); (b) mixing of mantle- and crust-derived components (Keay et al., 1997; Kemp et al., 2007); and (c) partial melting of crustal rocks with heat and water input from basaltic magmas emplaced beneath the lower crust (Annen et al., 2006; Collins et al., 2016). Scenario (a) can be eliminated because experimental studies have shown that direct melting of mantle-derived basaltic magma is not capable of forming quartz-saturated felsic magma (Campbell et al., 2014). Researchers generally agree that if granitic magmas are generated by direct fractional crystallization of mantle-derived magma, a complete evolutionary sequence of mafic to felsic rocks should have existed (e.g., Turner et al., 1992; Mushkin et al., 2003; Litvinovsky et al., 2015). However, in the study area, intermediate and felsic rocks are substantially more abundant than mafic rocks (Figs. 1c and 2), reflecting an unlikely scenario of fractional crystallization. Furthermore, absence of mafic microgranular enclaves and mafic compositions in the Tantoushan monzogranites excludes the likelihood of scenario (b).

The Tantoushan monzogranite samples display significant enrichment in Rb, Th, U, K, and Pb and pronounced depletion in Ba, Sr, P, Ti, and Eu (Fig. 9). In addition, the monzogranite samples contained 75.30–76.98 wt% SiO_2, with MgO contents (0.03–0.12 wt%) and $Mg^{\#}$ values (4.50–11.96) lower than those of the lower crust (7.24 wt% MgO, $Mg^{\#}$ = 60.1) (Rudnick and Gao, 2003). The Ti/Zr, Ti/Y, and La/Nb ratios of the samples are 1.61–4.31, 4.23–27.35, and 0.27–2.22, respectively, comparable to the ratios of typical crust-sourced rocks (Ti/Zr < 20, Ti/Y < 200, and La/Nb = 1.7) (Taylor and McLennan, 1995; Wedepohl, 1995). Other geochemical signatures suggestive of crustal sources include low Nb/Ta (7.97–10.64), Zr/Hf (20.99–33.40), Nb/U (3.34–8.38), and Ta/U (0.41–0.88) ratios, similar to those of crustal rocks (Nb/Ta = 11.4, Zr/Hf = 33.0, Nb/U = 12.1, and Ta/U = 1.1) but lower than those of mantle-derived rocks (Nb/Ta = 17.8, Zr/Hf = 37, Nb/U = 47, and Ta/U = 2.7) (Hofmann et al., 1986; McDonough and Sun, 1995; Taylor and McLennan, 1995; Rudnick and Gao, 2003). Moreover, studied samples have relatively high Th/Ce (0.50–1.42), Th/La (0.98–3.05), Lu/Yb (0.16–0.17), and Rb/Sr (5.28–51.71) ratios, which are distinctly higher than those of the primitive mantle (Th/Ce = 0.02–0.05, Th/La = 0.12, Lu/Yb = 0.14–0.15, and Rb/Sr = 0.03–0.047) (Sun and McDonough, 1989; Rudnick and Gao, 2003), but similar to the values of the crust (Th/Ce ≥ 0.15, Th/La > 0.30, Lu/Yb = 0.16–0.18, and Rb/Sr > 0.5) (Sun and McDonough, 1989; Rudnick and Gao, 2003; Plank, 2005). In addition to geochemical evidence, the Hf isotope composition also suggests a crustal source for the monzogranites. The Hf isotope analyses of zircons from the Tantoushan monzogranites have negative $\varepsilon_{Hf}(t)$ values ranging from −17.7 to −8.6, and old two-stage Hf model ages (T_{DM2}(Hf)) in the range of 1807–2378 Ma, indicating their derivation from the partial melting of the Paleoproterozoic lower crust (Fig. 7), in agreement with earlier findings (Zhao et al., 2005; Peng, 2015). Zhao et al. (2005) pointed out that the Archean continental crust in the northern NCC had been rejuvenated by the underplating of mafic magmas at approximately 1.8 Ga, which is likely related to the cratonization of the NCC. Peng et al. (2015) found that voluminous Paleoproterozoic mafic dike swarms (2.15–1.89 Ga) exist in the northern NCC, and the swarms and related magmatic series could constrain the tectonic evolution. The inconsistency between zircon Hf isotopic

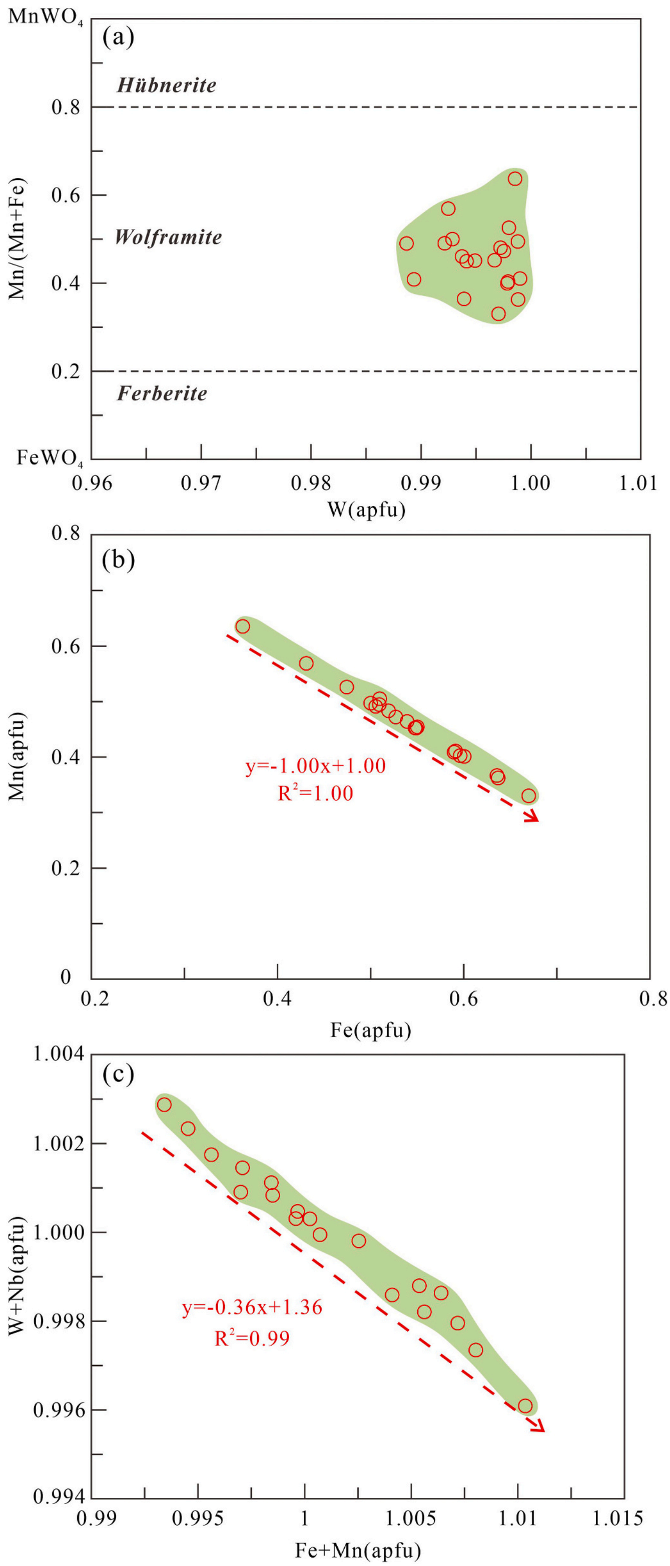

Fig. 10. Chemical variations in major and trace elements in wolframite of the Tantoushan W deposit. (a) Mn/(Mn + Fe) versus W diagram; (b) correlation between Mn and Fe contents in wolframite; (c) negative correlation between (W + Nb) and (Fe + Mn) contents.

compositions of the W-bearing monzogranite in Tantoushan and W-mineralized granitoids in NE China illustrates that the origin of monzogranite is different from the Jurassic and Early Cretaceous W-mineralized granitoids in NE China, and the latter mainly originated from partial melting of juvenile lower crustal materials with $\varepsilon_{Hf}(t)$ and T_{DM2}(Hf) ranging from −2.6 to 18.3 and 1378–303 Ma, respectively (Table S3 and Fig. 7).

Fractional crystallization likely occurred during the formation of Tantoushan monzogranites as the samples were plotted into the field of highly fractionated granites (EI Bouseily and EI Sokkary, 1975) based on Rb, Sr, and Ba contents (Fig. 8d). Moreover, in the (K_2O + Na_2O)/CaO versus Zr + Nb + Ce + Y diagram (Fig. 12a), all samples are plotted in the highly fractionated granite field rather than in the unfractionated I- and S-type granite field. They also have wide ranges of Zr (123–233 ppm) and Sm (10.30–47.60 ppm) concentrations, but relatively consistent Zr/Nb (3.09–8.27) and La/Sm (3.97–9.67) ratios (Allègre and Minster, 1978), which indicates that the magma underwent extreme fractional crystallization. In the chondrite-normalized REE patterns, significantly negative Eu anomalies (Eu/Eu* = 0.05–0.29) reflect fractional crystallization of plagioclase and/or K-feldspar (Fig. 9a). In the primitive mantle-normalized trace element diagrams (Fig. 9b), pronounced depletions in Ba, Sr, P, and Ti may reflect the separation of plagioclase, K-feldspar, Ti-bearing minerals, and apatite. These lines of evidence collectively indicate that the parent magmas of the monzogranites underwent extensive fractional crystallization. In summary, we propose that the monzogranites from the Tantoushan deposit are highly fractionated I-type granitoids, which were derived from the partial melting of the Paleoproterozoic lower crust and subsequently experienced significant fractional crystallization processes.

6.3. Factors controlling trace element compositions of wolframite

Wolframite is the most significant W-bearing mineral in quartz-wolframite vein-type deposits. Hence, studying the geochemical signature of wolframite provides an efficient approach for revealing the delicate wolframite forming processes, which is critical for understanding W-related magmatic-hydrothermal systems (Harlaux et al., 2018; Deng et al., 2019; Xiong et al., 2020).

Wolframite is a typical ABO_4 compound with two octahedral sites (A and B) (Shannon, 1976). The wolframite structure is versatile and allows for multiple isovalent substitutions (Beddoestephens and Fortey, 1981; Polya, 1988; Černý and Ercit, 1989; Tindle and Webb, 1989; Tindle et al., 1998; Černý et al., 2007; Goldmann et al., 2013; Harlaux et al., 2018; Deng et al., 2019). Due to similar ionic radii of Fe^{2+} (0.78 Å) and Mn^{2+} (0.83 Å) in octahedral coordination (Shannon, 1976), the contents of Fe and Mn in the wolframite samples show a typical linear trend with a slope of −1.00, indicating an evident substitution of isovalent $Fe^{2+} \leftrightarrow Mn^{2+}$ (Fig. 10b). In the studied samples, the contents of W + Nb and Fe + Mn commonly display a clearly negative correlation (R^2 = 0.99) (Fig. 10c). Several correlations among the trace elements in wolframite are discriminable from binary diagrams. For instance, Fig. S1a shows that the Nb and Ta contents of wolframite correlate, indicating that Nb and Ta were incorporated together during wolframite crystallization. Trivalent cations (Sc^{3+}, V^{3+}, and Y^{3+}) are positively correlated with each other (Fig. S1b–d); they also correlate positively with Nb and Ta (Fig. S1e–h), implying that these elements were incorporated through a similar mechanism during the crystallization of wolframite. These correlations between the elements in wolframite, shown in the binary diagrams, may be explained by the substitution mechanism of Eq. (1) (Polya, 1988; Tindle and Webb, 1989):

$$^{A}(Fe,Mn)^{2+} + {}^{B}W^{6+} \leftrightarrow {}^{A}M^{3+} + {}^{B}(Nb,Ta)^{5+} \quad (1)$$

where M^{3+} are the trivalent cations (Sc^{3+}, V^{3+}, and Y^{3+}), and A and B are the two octahedral sites in wolframite (ABO_4; A = Fe^{2+}, Mn^{2+}; B = W^{6+}). Another substitution reaction (Eq. (2)) was also proposed (Černý et al., 2007). This reaction assumes that there are structural vacancies (□) that can compensate for each other.

$$^{A}(Fe,Mn)^{2+} + {}^{B}\square + 3{}^{B}W^{6+} \leftrightarrow {}^{A}\square + 4{}^{B}(Nb,Ta)^{5+} \quad (2)$$

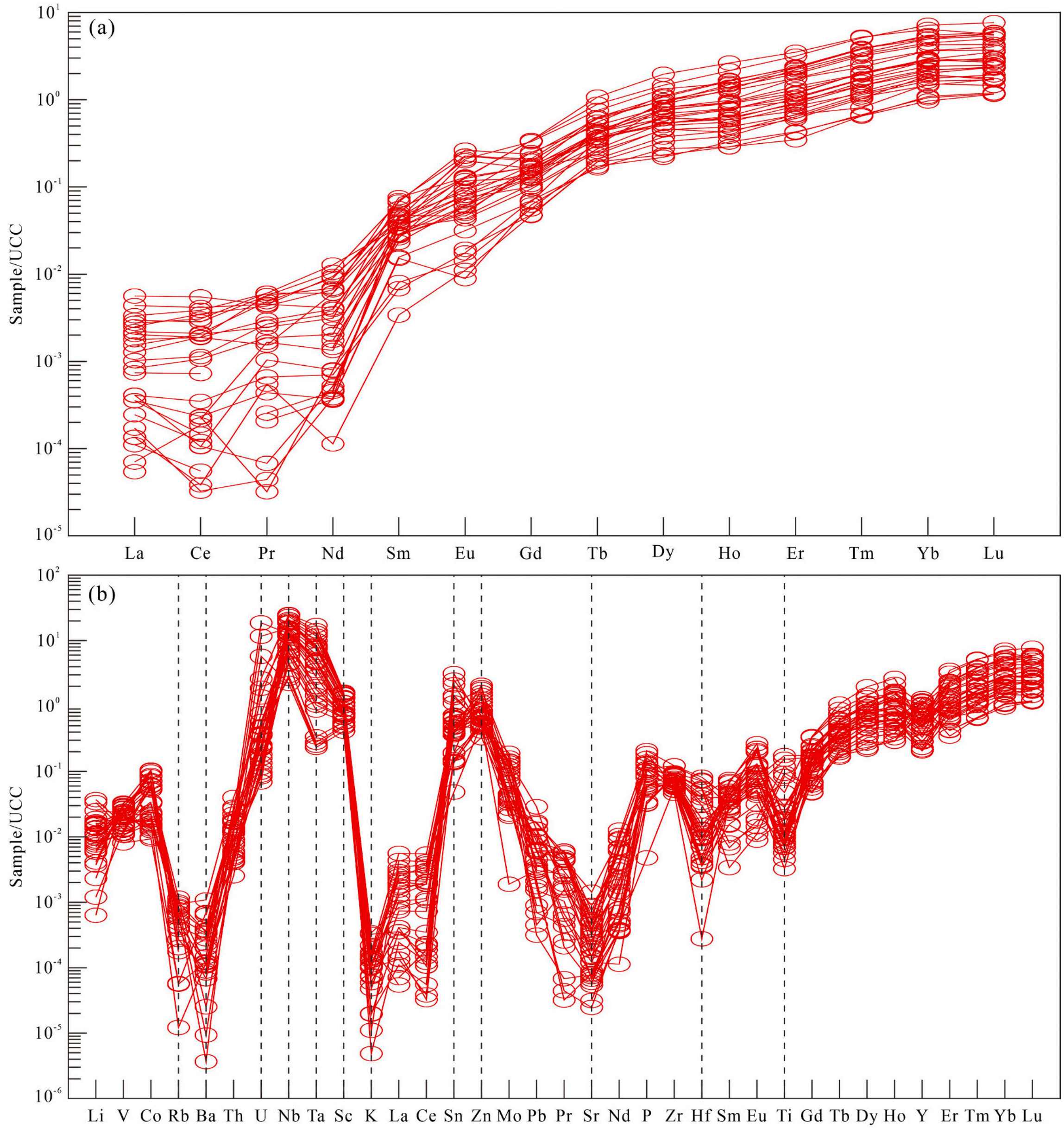

Fig. 11. REE (a) and trace elements (b) patterns of wolframite from the Tantoushan W deposit normalized to the upper continental crust (UCC from Rudnick and Gao, 2003).

Tetravalent cations (Ti^{4+}, Sn^{4+}, Zr^{4+}, and Hf^{4+}) are positively correlated with each other (Fig. S2a–f) and with trivalent cations (Sc^{3+}, V^{3+}, and Y^{3+}) (Fig. S2g–l), indicating that they were likely incorporated into the wolframite lattice via a common mechanism. The chemical variations described above can be tentatively explained by Eqs. (3) and (4) (Tindle and Webb, 1989; Harlaux et al., 2018):

$$2^{A}(\mathrm{Fe,Mn})^{2+} + {}^{B}\mathrm{W}^{6+} \leftrightarrow 2^{A}\mathrm{M}^{3+} + {}^{B}\mathrm{N}^{4+} \tag{3}$$

$$^{A}\square + {}^{B}\mathrm{W}^{6+} \leftrightarrow {}^{A}(\mathrm{Fe,Mn})^{2+} + {}^{B}\mathrm{N}^{4+} \tag{4}$$

where N^{4+} represents the tetravalent cations (Ti^{4+}, Sn^{4+}, Zr^{4+}, Hf^{4+}). In addition, the Nb content of wolframite in this study shows positive correlations with Ti, Sn, Zr, and Hf (Figs. S2m–p), implying that these elements were also incorporated into the wolframite lattice via a similar mechanism, as expressed by the coupled substitution reaction of Eq. (5) (Tindle and Webb, 1989):

$$^{A}(\mathrm{Fe,Mn})^{2+} + 2^{B}\mathrm{W}^{6+} \leftrightarrow {}^{A}\mathrm{N}^{4+} + 2^{B}(\mathrm{Nb,Ta})^{5+} \tag{5}$$

Based on these findings, it can be concluded that the trace element compositions of wolframite from the Tantoushan deposit were controlled by the crystallochemical effects and that five isovalent substitution mechanisms could potentially explain the observed trace element variations in wolframite. Considering that the five substitution mechanisms occurred simultaneously during wolframite formation, they can be unified as shown in Eq. (6):

$$4^{A}(\mathrm{Fe,Mn})^{2+} + 8^{B}\mathrm{W}^{6+} + {}^{B}\square \leftrightarrow 3^{A}\mathrm{M}^{3+} + {}^{A}\mathrm{N}^{4+} + 7^{B}(\mathrm{Nb,Ta})^{5+} + 2^{B}\mathrm{N}^{4+} \tag{6}$$

Previous studies revealed that the crystallochemical effects and composition of the primary mineralizing fluids are key factors controlling the chemistry of wolframite, and that the Y/Ho and Zr/Hf ratios define the charge and radius controlled (CHARAC) behavior of common igneous rocks and wolframite (Bau, 1996; Harlaux et al., 2018; Xiong et al., 2020, 2021). In the Y/Ho versus Zr/Hf diagram, almost all studied wolframite samples fall outside the CHARAC field (Fig. 13a), indicating that the ionic radius and the charge valence are not the only parameters

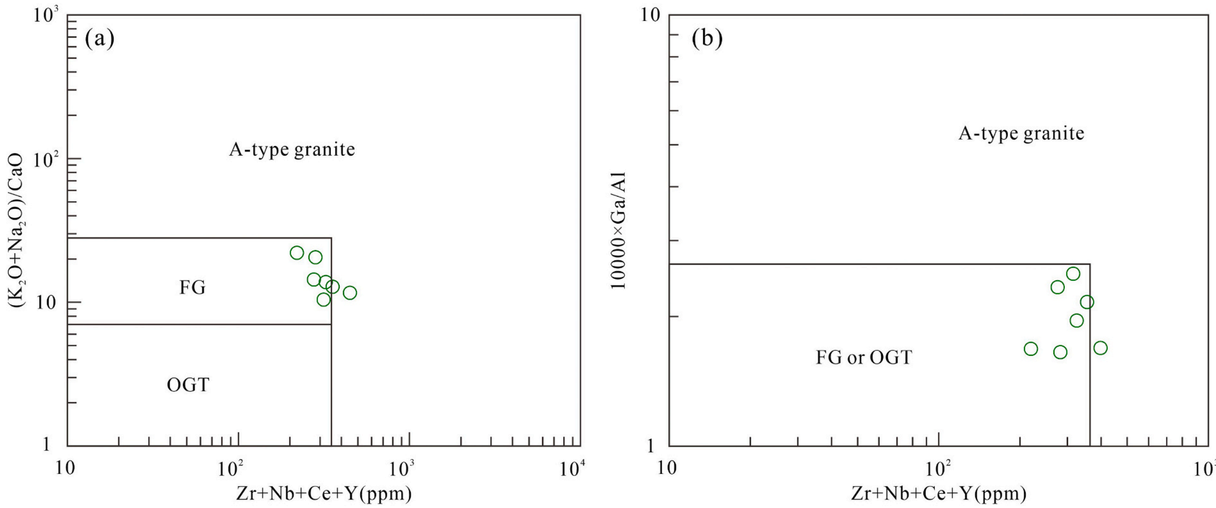

Fig. 12. (a) (K_2O + Na_2O)/CaO, and (b) 10,000 × Ga/Al versus (Zr + Nb + Ce + Y) diagram of Whalen et al. (1987). Abbreviations are as follow: FG: highly fractionated granite; OGT: unfractionated I- and S-type granite.

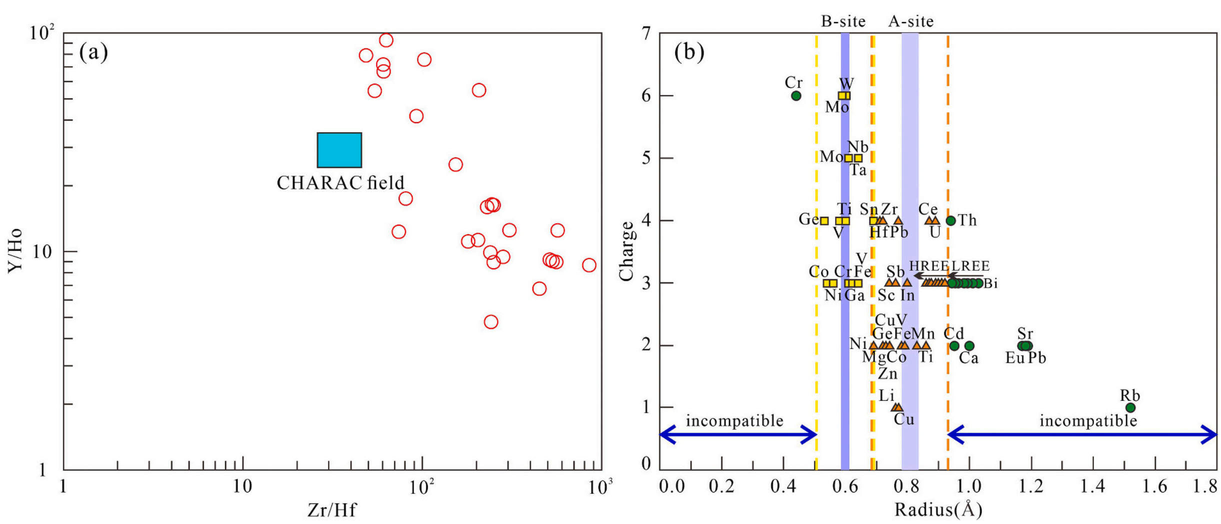

Fig. 13. (a) Y/Ho versus Zr/Hf ratios in wolframite from the Tantoushan deposit. The CHARAC field is from Bau (1996). (b) Ionic radius versus electric charge diagram for major and trace elements in octahedral coordination in wolframite showing the theoretical occupancy of the A- and B-sites (modified from Harlaux et al., 2018). Dash lines represent the lower and upper limits of 15 % relatively to the lattice site radius corresponding to total substitution (Goldschmidt's rule). Ionic radii data are from Shannon (1976).

controlling the partitioning of trace elements from fluids into wolframite. Thus, the concentrations of the trace elements incorporated during the crystallization of hydrothermal wolframite also reflect the specific chemical compositions of the ore-forming fluids. The wolframite from Tantoushan is characterized by enrichments in Ti, Sc, Zn, Y, Zr, Nb, and HREEs with concentrations ranging from 10 to 10^3 ppm, and by depletions in V, Cr, Ni, Sn, Ta, and U with concentrations ranging from 0.01 to 10 ppm. The similar geochemical signatures of trace elements measured for different wolframite samples may indicate an additional control of the composition of primary mineralizing fluids on the trace element composition of wolframite. The high concentrations of Sc, Zn, Y, Zr, and Nb in wolframite indicate that these elements are efficiently incorporated into the crystal structure of wolframite. The low concentrations of other elements (e.g., Cr, Ni, LREEs, and U) indicate that they are either not prone to be incorporated into wolframite or are present at very low concentrations in the mineralizing fluids owing to their low solubility in aqueous solutions. The diagram of ionic radius versus electric charge (Fig. 13b) shows that the low concentrations of many trace elements in wolframite can be potentially explained by crystallochemical control. For instance, the preferential enrichment in HREEs compared to LREEs observed for all wolframite samples (Fig. 11a) is likely due to crystallochemical constraints. Similar observations have been reported in previous studies of wolframite geochemistry (Gan and Chen, 1992; Goldmann et al., 2013; Xiong et al., 2017, 2020; Harlaux et al., 2018; Zhang et al., 2018). The preferential incorporation of HREEs is likely due to the very similar ionic radii of HREEs (Gd^{3+}: 0.94 Å; Lu^{3+}: 0.86 Å) to those of Fe^{2+} (0.78 Å) and Mn^{2+} (0.83 Å) in octahedral coordination on the A-site (Shannon, 1976) (Fig. 13b). In contrast, scheelite tends to preferentially incorporate LREEs (Raimbault et al., 1993; Ghaderi et al., 1999), which have similar ionic radii (La^{3+}: 1.03 Å; Eu^{3+}: 0.95 Å) to Ca^{2+} (1.0 Å) in octahedral coordination (Shannon, 1976). In addition, Rb^{+}, Sr^{+}, Eu^{2+}, Pb^{2+}, Cd^{2+}, and Bi^{3+} are unable to enter the A-site because of their large ionic radii (>0.92 Å), whereas Cr^{3+} (0.61 Å) can possibly enter the B-site of the wolframite structure but not Cr^{6+} because of its small ionic radius (<0.56 Å). Theoretically, charge-compensating elements such as Cu^{+}, Li^{+}, and Sb^{3+} can enter the A-site relatively easily. However, these elements are not systematically detected in wolframite, which may reflect a primary depletion of those elements in the source magmas and the hydrothermal ore-forming fluids.

In summary, the crystallochemical effects and composition of the initial hydrothermal fluids are two key factors controlling the trace element compositions of wolframite from the Tantoushan deposit.

6.4. Genetic link between the W-bearing monzogranites and W mineralization

The Triassic W-bearing and W-barren granites commonly coexist spatially, and it is often difficult to distinguish them by petrographic studies. By comparing their geochemical compositions, it is possible to gain an insight into the likely control of W- fertile and barren magmas, thereby providing a better understanding of the relationship between W-bearing granites and W mineralization. As previously mentioned, compared to the Triassic W-barren granitoids in NE China, the Tantoushan W-bearing monzogranites are characterized by low LREE/HREE ratios and significantly negative Eu anomalies, indicating that the Tantoushan W-bearing monzogranites have a higher degree of fractionation than the Triassic W-barren granitoids (Miller and Mittlefehldt, 1982, 1984). In addition, the degree of magmatic fractionation can also be monitored by the Rb/Sr, Nb/Ta, Zr/Hf, and K/Rb ratios, which are considered as 'geochemical twins' because these elements have the same charges and ionic radii, similar geochemical properties, and are expected to experience very minor fractionation during most geological processes (Green, 1995). Previous studies demonstrated that the Rb/Sr ratios would increase, whereas the Nb/Ta, Zr/Hf, and K/Rb ratios would decrease with the evolving fractional crystallization of granites (Bau, 1996; Linnen and Keppler, 1997; Dostal and Chatterjee, 2000; Linnen and Keppler, 2002; Claiborne et al., 2006; Deering and Bachmann, 2010; Dostal et al., 2015; Ballouard et al., 2016). The Tantoushan W-bearing monzogranites have higher Rb/Sr ratios, and lower Nb/Ta, Zr/Hf, and K/Rb ratios than the Triassic W-barren granitoids in NE China (Fig. 14a–d), indicating the Tantoushan W-bearing monzogranites are more fractionated than contemporary W-barren granitoids.

In general, W mineralization is associated with highly fractionated granites, which is confirmed by many studies worldwide (Singh and Singh, 2001; Fogliata et al., 2012; Mao et al., 2013; Huang and Jiang, 2014; Zhang et al., 2017b; Cao et al., 2018b, 2020; Harlaux et al., 2018; Jiang et al., 2018; Yuan et al., 2018; Steiner, 2019; Wang et al., 2020b; Li et al., 2021a). It is proposed that ore-forming elements may be concentrated during multiple stages of magmatic activity and then extracted by magmatic fluids (Che et al., 2013; Harlaux et al., 2018) or leached from granitoids and/or metamorphic rocks and transported by external (metamorphic or meteoric) fluids (Linnen and Williams-Jones, 1995; Vindel et al., 1995; Vallance et al., 2001). These experimental studies focused on the partition coefficients between minerals and fluid/melts (Che et al., 2013), analyses of fluid inclusions (Wei et al., 2012; Li et al., 2018; Pan et al., 2019; Ni et al., 2020), geochronology of W deposits and their host granites (Li et al., 2021b; Xie et al., 2022a), and geochemical analyses of mineral elemental and stable isotope compositions (Xiong et al., 2017; Harlaux et al., 2018; Zhang et al., 2018; Legros et al., 2019; Li et al., 2021a), which confirmed that the enrichment of W and other incompatible elements during magmatic fractionation is an essential requirement for the formation of W mineralization. By comparing the geochemical compositions of Mesozoic W-mineralized and W-barren granitoids, Xie et al. (2021b) concluded that the Mesozoic W-mineralized granitoids have higher W concentrations, Rb/Sr, and U/Th ratios, but lower $(La/Yb)_N$, LREE/HREE, Eu/Eu*, K/Rb, Zr/Hf, Nb/Ta, and Y/Ho ratios than contemporary W-barren granitoids. In the present study, the Triassic Tantoushan W-bearing monzogranite samples are mostly plotted in the field of Mesozoic W-mineralized granitoids, whereas contemporary W-barren granitoids all fall into the field of Mesozoic W-barren granitoids (Xie et al., 2021b) (Fig. 14a–d). Using Rb/Sr as a parameter to measure the extent of magma fractionation, Lehmann (1987) and Lehmann et al. (1990) stressed that extreme fractional crystallization may result in both very high Rb/Sr ratio and elevated W concentrations in the magmas, which is a critical process for the formation of W deposits. It is noteworthy that the Tantoushan W-bearing monzogranite contains higher W concentrations than contemporary W-barren granitoids and the average continental crust (Fig. 14e, f). In combination with published geochemical data of Mesozoic W-mineralized granitoids, it is notable that the W concentrations of W-mineralized granitoids increase with increasing Rb/Sr ratios (Fig. 14e) and decrease with increasing K/Rb ratios (Fig. 14f), suggesting that fractional crystallization of the W-mineralized granitic magma enhances the enrichment of W in magmas. In addition, the lower intercept $^{206}Pb/^{238}U$ age of wolframite agrees well with the zircon weighted average mean $^{206}Pb/^{238}U$ age of the W-bearing monzogranite, further demonstrating the genetic correlation between them.

In summary, the extreme fractional crystallization of the W-bearing monzogranites in Tantoushan may have resulted in the enrichment of W and related incompatible elements, which are necessary for the formation of W mineralization. The highly fractionated Tantoushan W-bearing monzogranite is likely the main source of metals for the formation of the Tantoushan deposit. The contemporary W-barren granitoids are irrelevant to the W mineralization probably because of their low fractionated signatures.

Based on the geological, geochronological, and geochemical features of the W-bearing monzogranites and wolframite from the Tantoushan deposit in NE China, we propose an integrated model of granitic magmatism and W mineralization in the Tantoushan ore district. During the Late Triassic, mantle-derived mafic magmas successively underplated beneath the ancient lower crust and induced extensive crustal melting, which produced a deep hot zone and generated felsic magmas. The mantle-derived mafic magmas halted as a result of obstruction by the deep hot zone and rarely passed through the zone (Annen et al., 2006), which may explain the rare exposure of contemporaneous mafic rocks in this area. Tungsten as a lithophile element is generally enriched in the crust but depleted in the mantle (Rudnick and Gao, 2003; Arevalo and McDonough, 2008). Thus, the Paleoproterozoic lower crust beneath the Tantoushan area may represent a significant potential source for W mineralization. Continual fractional crystallization appears to have been the dominant process that further enriched W in granitic magmas. Previous studies confirmed the importance of magmatic differentiation in the formation of W deposits, through which ore metals (W) and volatiles (F) are enriched in the highly evolved magma and then accumulate in the residual liquid (Thomas et al., 2005; Romer et al., 2014; Li et al., 2021a). Similarly, the highly fractionated I-type granitoids in the Tantoushan area contributed to W enrichment. In the late stage of magma evolution, volatile-rich fluids were exsolved and segregated from the melt. Their subsequent liquid-vapor phase separation could have changed the physical and chemical conditions of the magmatic-hydrothermal system (Li et al., 2021a). The post-magmatic fluids became enriched in F and Cl, along with the improved solubility of W (Webster and Holloway, 1988; Keppler and Wyllie, 1991; Schaller et al., 1992; Signorelli and Carroll, 2000; Zajacz et al., 2008; Yuan et al., 2019). Previous studies demonstrated that W could strongly partitioned from the melt into the fluid during the magmatic-hydrothermal transition (Gibert et al., 1992; Wood and Samson, 2000). Along with changes in temperature and pressure gradients, the ore-bearing hydrothermal fluids migrated along a series of NNE-trending faults in the Tantoushan area. Infiltration and metasomatism occurred continuously between the W-bearing hydrothermal fluids and country rock, finally leading to the precipitation of W owing to favourable physical and chemical conditions. During the crystallization of wolframite, trace elements selectively entered into the wolframite lattice under the control of the crystallochemical parameters and the composition of hydrothermal ore-forming fluids.

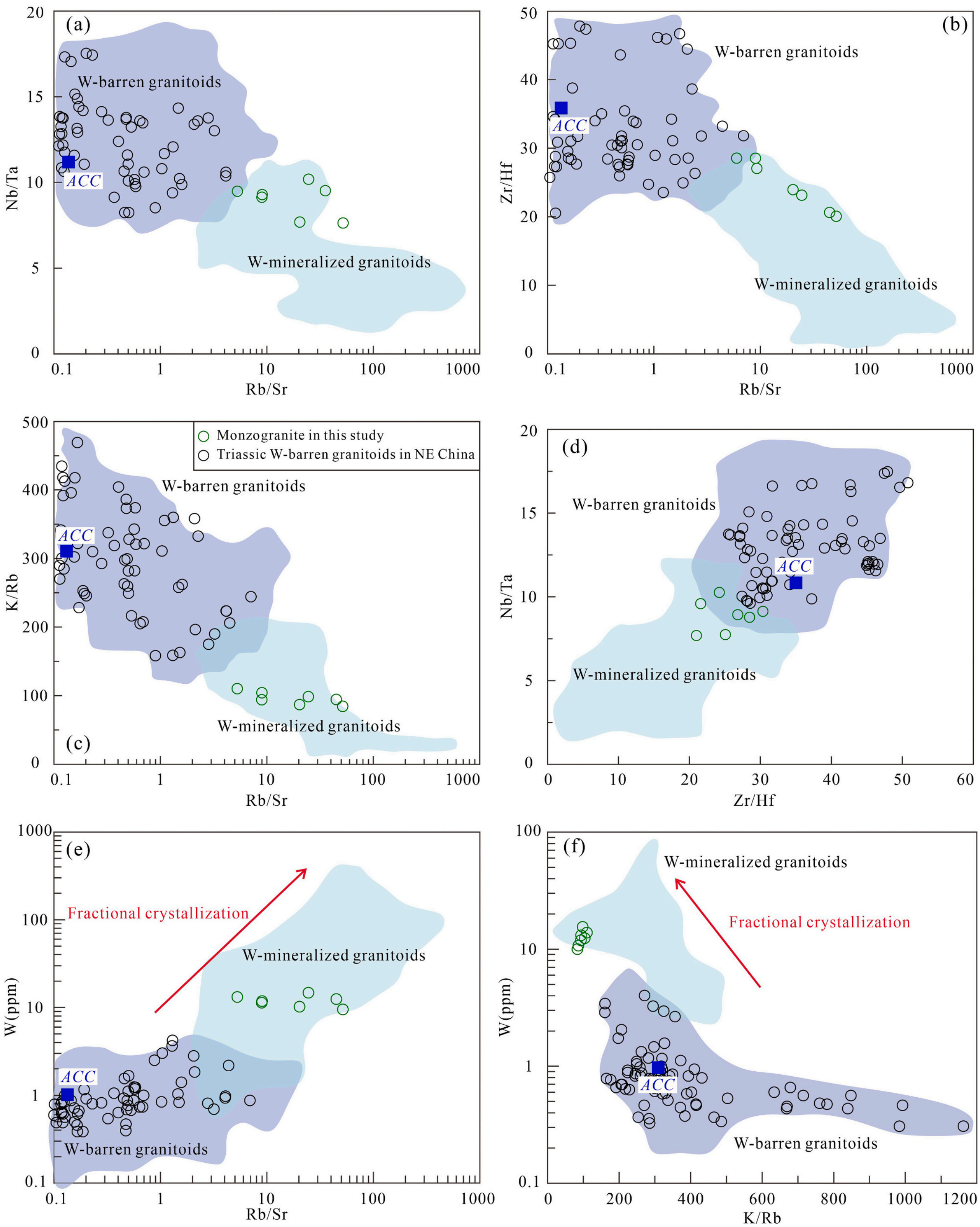

Fig. 14. (a) Nb/Ta versus Rb/Sr diagram. (b) Zr/Hf versus Rb/Sr diagram. (c) K/Rb versus Rb/Sr diagram. (d) Nb/Ta versus Zr/Hf diagram. (e) W versus Rb/Sr diagram. (f) W versus K/Rb diagram. Data for Triassic W-barren granitoids in NE China are listed in Table S4. Field for average continental crust (ACC) is from Rudnick and Gao, 2003, and fields for Mesozoic W-mineralized and W-barren granitoids in NE China are from Xie et al., 2021.

6.5. Tectonic implications

The formation of Triassic W-related granitoids and associated W mineralization in NE China is related to regional large-scale tectonic-magmatic-hydrothermal activity (Wang et al., 2021; Xie et al., 2021b). Hence, understanding the Triassic tectonic evolution in NE China is essential to gain insights into the formation of W-related granitoids and the associated W mineralization in this area. Below is our interpretation of the tectonic control on the Triassic W metallogeny in NE China based on this case study and previous studies.

Although the disappearance of the PAO occurred along the SXCF, its closure time remains controversial (Eizenhöfer et al., 2014; Liu et al., 2017). Liu et al. (2017) systematically summarized the available reported data and different models for the Paleozoic tectonic evolution of the easternmost CAOB, concluding that the final closure of the PAO occurred along the SXCF with a scissor-style closure from the Late Permian to Early Triassic in the west to Late Permian–Middle Triassic in the east. The presence of the Xilingol Complex, terrestrial Linxi Formation deposition (Li et al., 2014b), collisional-related granites (Chen et al., 2009), and Wudaoshimen ophiolite (Wang et al., 2014) support this interpretation. Moreover, existing geological evidence suggests that melting of the thickened lower crust occurred because of amalgamation of the NE China blocks and NCC during the subduction of the PAO, which induced the formation of granitic parental magmas for W mineralization in this area, including the Middle Permian–Early Triassic syn-collisional granitoids in the eastern Jilin Province (Cao et al., 2013), Late Permian I-type granitoids along the SXCF (Sun et al., 2004), Triassic mafic volcanics and lacustrine molasses in the SGB (Zhang et al., 2008a), granodiorites in the Baiyinnuoer area (SGB; 245 Ma) (Jiang et al., 2017), Middle Triassic tonalities in the central Great Xing'an Range (GXR) (234–240 Ma) (Jiang et al., 2011), Early–Middle Triassic syn-collisional S-type granitoids in Linxi (SGB) and the Horqin right wing middle banner (the central GXR) (Li et al., 2007; Zhang et al., 2015), and synchronous adakitic plutons in the Yanbian fold belt (251–240 Ma) (Ma et al., 2017). Furthermore, the final closure stage of the PAO is marked by an extensional setting represented by the occurrence of Late Triassic bimodal volcanics (217–202 Ma) (Wang et al., 2015), A-type granitic (Gou et al., 2013), and rhyolitic rocks (Xu et al., 2013b; Guo et al., 2015) in the Lesser Xing'an-Zhangguangcai Range. Shang (2004) reported radiolarians in the argillite bed of the Zhesi Formation from the Middle Permian in the Zhesi and Xilinhot areas. This finding indicates that deep marine sedimentary facies persisted during the Middle Permian and that the ocean between the NCC and SC, probably extending along the Linxi ophiolite belt, was not closed until the Late Guadalupian (~270–250 Ma). Han et al. (2015) reported the youngest detrital zircon U-Pb age of 238 Ma from the Linxi Formation in the Linxi area, indicating that the final closure of the PAO occurred in the Early Triassic. Detrital zircon U-Pb dating of the Xingfuzhilu Formation in southern Inner Mongolia suggests that a closed remnant ocean basin possibly existed in the Middle Permian immediately prior to the final collision of the CAOB and closure of the PAO (Li et al., 2014a). The reported paleomagnetic data also provide further constraints on the final closure of the PAO. According to paleomagnetic data, Li et al. (2006) concluded that the SC began to rapidly drift southward in the Early Permian and collided with the NCC at the end of the Permian (250 Ma). Rock magnetic and paleomagnetic studies of Permian sandstone from the Taohaiyingzi area in Inner Mongolia indicated that the area amalgamated with the NCC during the Late Permian (Qin et al., 2013). The final closure of the PAO primarily influenced the southernmost region of NE China and the northern margin of the NCC (Mao et al., 2020) (Fig. 15a).

The Tantoushan monzogranites comprise high-K calc-alkaline granitoids (Fig. 8b), which typically form in active continental margins or post-collisional settings (Condie, 1976; Pitcher, 1987; Liegeois, 1998). Pearce et al. (1984) found that granites from different tectonic settings had different (Y + Nb), (Yb + Ta), and Rb contents. Our samples are plotted in the overlapping post-collision and syn-collision granite fields in the Rb versus (Y + Nb) and (Yb + Ta) diagrams (Fig. 16a and b), suggesting that they may have formed in a collision-related setting. In the R2 versus R1 diagram (Batchelor and Bowden, 1985), the samples mainly fall in or near the post-collision domain (Fig. 16c), indicating a post-collision-related setting. In the Rb/30–Hf–3Ta discrimination diagram (Harris et al., 1986), most samples are plotted in the post-collision field (Fig. 16d), further implying a post-collision-related setting. These characteristics suggest that the Tantoushan monzogranites may have been emplaced in a post-collision extensional setting.

The studies above clearly indicate that the PAO closure had a long history throughout the Paleozoic until the early Mesozoic, which involved subduction/accretion processes on the northern margin of the NCC and the southern margin of NE China during the Paleozoic and a final collision along the SXCF during the Late Permian–Early Triassic times in the west. We therefore conclude that the Tantoushan monzogranites and related W deposit formed in a post-orogenic extensional setting controlled by the closure of the PAO (Fig. 15b).

6.6. Implication for regional W exploration

Romer and Kroner (2016) stressed that the formation of Sn and/or W mineralization can be a sequence of processes, including source enrichment and accumulation of ore-forming materials and metal extraction. In the metal extraction process, different tectonic settings may involve input of mantle melt or emplacement of ultrahigh-temperature metamorphic rocks, which act as fertile source rocks and play an important role in controlling the heterogeneous distribution of W mineralization within metallogenic belts. Therefore, a full understanding of metallogenic tectonic settings is critical for regional W exploration. As previously mentioned, to date, only three W deposits (Shazigou, Yangjingou, and Tantoushan) have been confirmed to be of the Triassic age according to their geochronological data, and they are all distributed along the SXCF. The Shazigou W-Mo deposit has a molybdenite mean Re-Os age of 243.8 ± 1.6 Ma, which is regarded to be formed in the Middle Triassic and in a syn- to post-collision setting following the closure of the PAO (Peng et al., 2015). The Yangjingou W deposit, situated in the western part of the SXCF, has a muscovite ^{40}Ar-^{39}Ar age of 230.8 ± 1.2 Ma (Late Triassic) (Zhao, 2014), which was formed in a post-collision extensional setting related to the closure of the PAO. In this study, the Tantoushan deposit was interpreted to form in a post-collision extensional setting following the closure of the PAO. Thus, we propose that all Triassic W deposits in NE China reported so far were formed in collision or extension settings related to the closure of the PAO.

Previous studies have demonstrated the importance of magmatic differentiation in the formation of W deposits, where ore metals (W) and volatiles (F and Li) become enriched in highly evolved magma, followed by accumulation in residual liquid (Thomas et al., 2005; Romer et al., 2014). The Tantoushan monzogranites are highly fractionated I-type granitoids. They have higher W concentrations, Rb/Sr ratios, and lower Nb/Ta, Zr/Hf, and K/Rb ratios than the Triassic W-barren granitoids in NE China (Fig. 14). These geochemical features suggest that highly fractionated granitoids are important prospective targets for future W exploration. The spatiotemporal distribution of the highly fractionated granitoids on both sides of the SXCF provides significant potential for W exploration, even though only the Tantoushan monzogranites have been demonstrated to be associated with W mineralization so far. In general, we suggest that the Triassic highly fractionated granitoids that experienced extreme magmatic differentiation and are distributed along the SXCF could be enriched in ore metals and volatiles, thereby representing potential targets for W mineralization.

7. Conclusions

(1) The zircon U-Pb dating defined an emplacement age of 233.1 ± 1.8 Ma for the W-bearing monzogranite in the Tantoushan

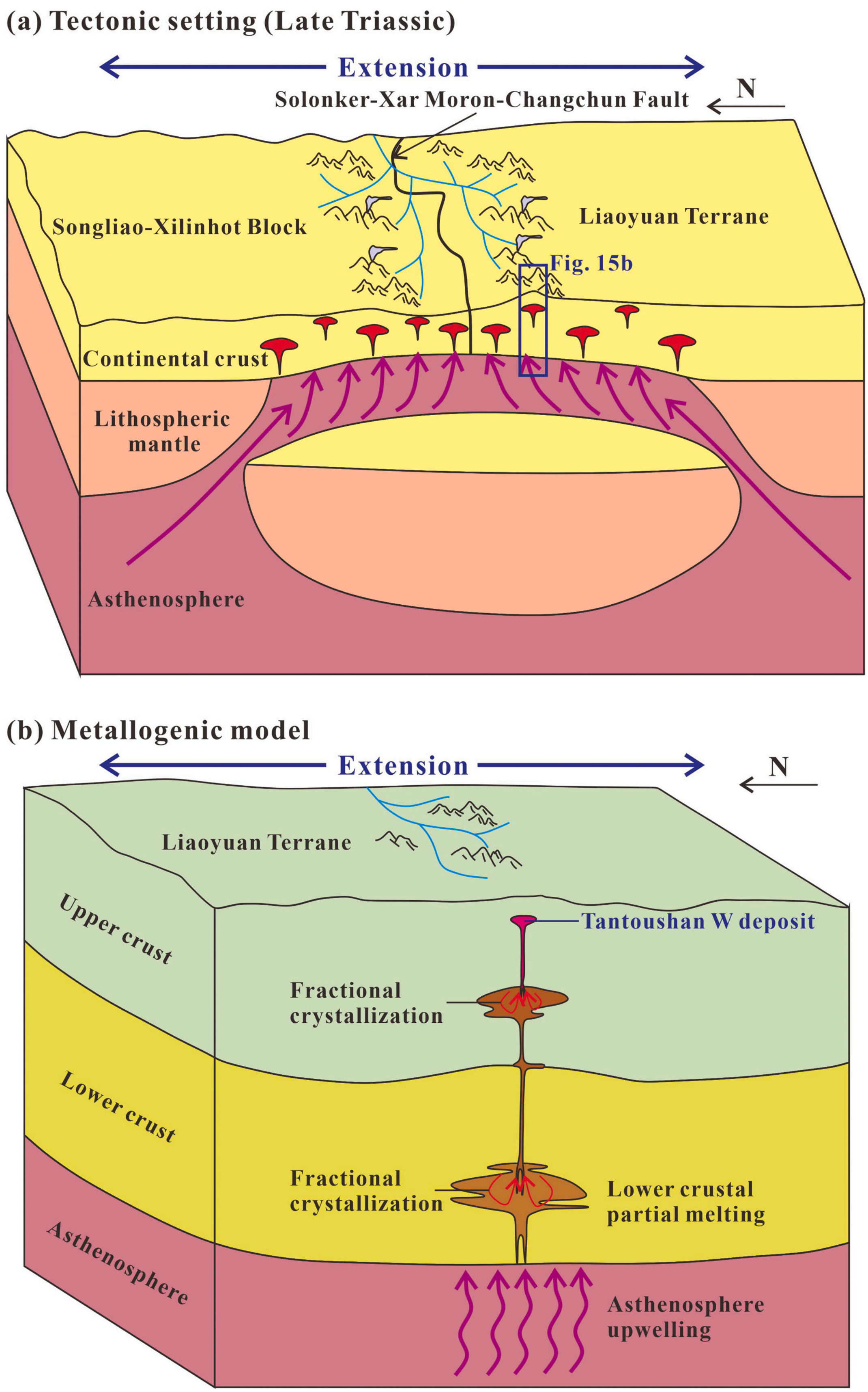

Fig. 15. (a) Sketches showing tectonic setting of the southwestern part of the NE China in Late Triassic (modified from Chen et al., 2020), and (b) the metallogenic model of the Tantoushan W deposit.

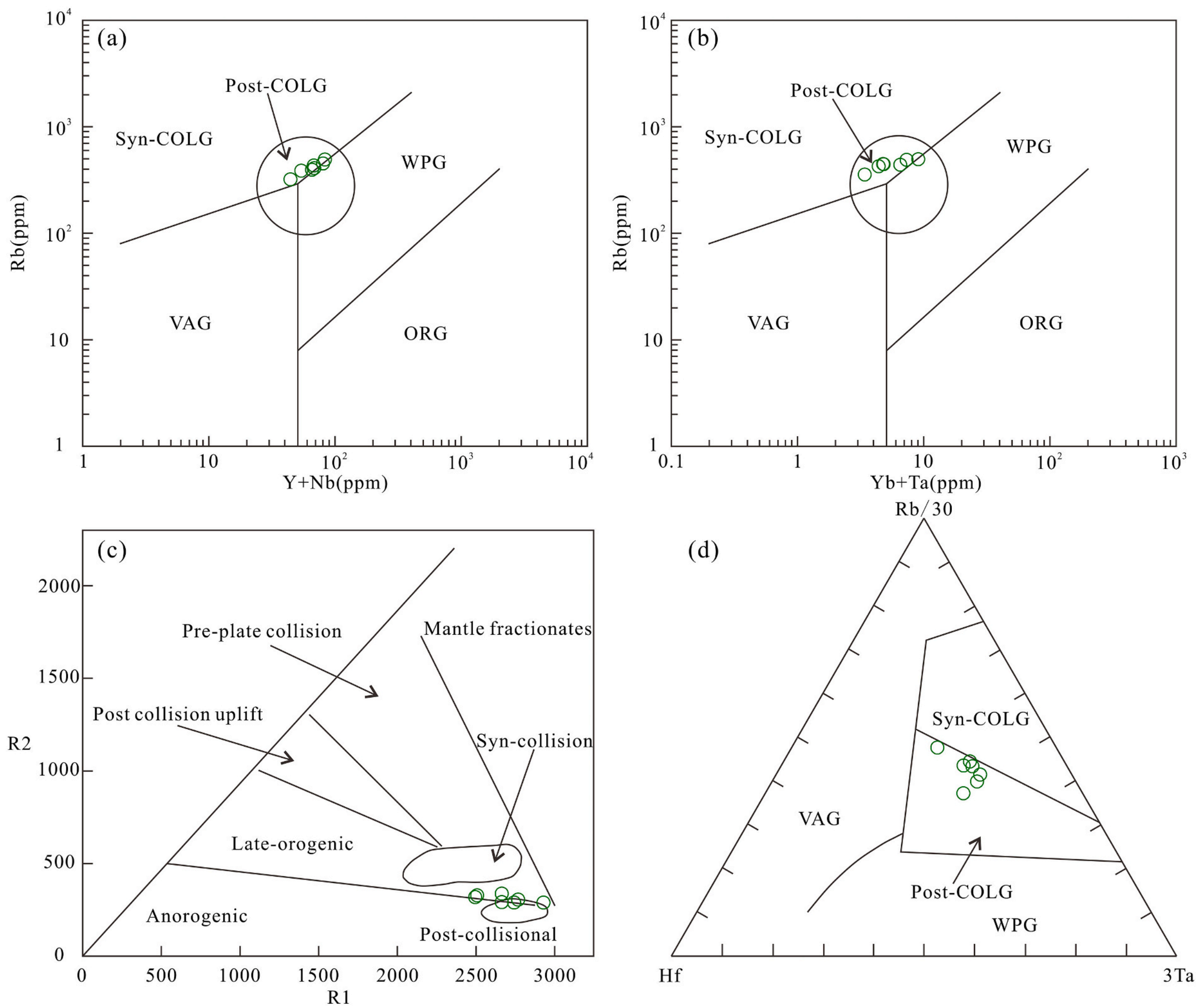

Fig. 16. (a) Rb versus (Y + Nb) diagram (after Pearce et al., 1984). (b) Rb versus (Yb + Ta) diagram (after Pearce et al., 1984). (c) R1 versus R2 diagram (after Batchelor and Bowden, 1985). (d) Rb/30–Hf–3Ta discrimination diagram (after Harris et al., 1986). Abbreviations are as follow: VAG = volcanic arc granite; ORG = ocean ridge granite; WPG = within plate granite; Syn-COLG = syn-collision granite; Post-COLG = post-collision granite.

deposit. *In situ* U-Pb dating of the wolframite yielded a lower intercept $^{206}Pb/^{238}U$ age of 234.3 ± 6.2 Ma, which is coeval within the analytical error with the spatially related monzogranitic intrusion. New geochronological data reported here provide clear evidence of a Late Triassic W-related magmatic-hydrothermal event in the Tantoushan area.

(2) The W-bearing monzogranites are highly fractionated I-type granitoids, mainly derived from the partial melting of the Paleoproterozoic lower crust that subsequently underwent extreme fractional crystallization processes. In contrast to the Triassic W-barren granitoids, the Tantoushan W-bearing monzogranites are characterized by high W concentrations, high Rb/Sr ratios, and low Nb/Ta, Zr/Hf, and K/Rb ratios. It appears that extreme fractional crystallization was critical for W enrichment in granitic magma. The W-barren granitoids did not induce W mineralization, likely because of their low fractionated signatures.

(3) The substitution reaction of $4^{A}(Fe, Mn)^{2+} + 8^{B}W^{6+} + {}^{B}\square \leftrightarrow 3^{A}M^{3+} + {}^{A}N^{4+} + 7^{B}(Nb, Ta)^{5+} + 2^{B}N^{4+}$ was demonstrated to play a critical role in the formation of hydrothermal wolframite from the Tantoushan deposit. The trace element compositions of wolframite were likely controlled by both crystallochemical parameters and the composition of primary mineralizing fluids.

(4) The Tantoushan deposit and genetically related monzogranites formed in a post-collision extensional setting controlled by the closure of the PAO. On both sides of the SXCF, Triassic highly fractionated granitoids have great potential for W mineralization, representing new exploration targets for granite-related W deposits.

Supplementary data to this article can be found online at https://doi.org/10.1016/j.gexplo.2022.107060.

Declaration of competing interest

The authors declare no conflict of interest.

Acknowledgements

We are grateful to the Profs. Stefano Albanese, Dave Lentz, and two anonymous reviewers for their constructive comments which greatly help in improving our paper. We would like to thank Drs. Hao Wang, Yue-Heng Yang, Lei Xu, Shi-Tou Wu and Bao-Quan Zhou from the State Key Laboratory of Lithospheric Evolution, Institute of Geology and Geophysics, Chinese Academy of Sciences for helping with zircon U-Pb dating and Hf isotope analyses. We would like to thank Yun-Ze Huang and Hong-Fang Chen from the Wuhan Sample Solution Analytical Technology Co., Ltd. for their help during the EPMA and LA-ICP-MS analysis of wolframite. We also thank Drs. Yan-Wen Tang and Jun-Jie

Han from the State Key Laboratory of Ore Deposit Geochemistry, Institute of Geochemistry, Chinese Academy of Sciences for help with *in situ* wolframite LA-SF-ICP-MS analysis. This work was financially supported by the National Natural Science Foundation of China (Grant No. 91962104) and the State Key Laboratory of Lithospheric Evolution, IGGCAS (SKL-Z201905).

References

Allègre, C.J., Minster, J.F., 1978. Quantitative models of trace element behavior inmagmatic processes. Earth Planet. Sci. Lett. 38, 1–25.

Annen, C., Blundy, J.D., Sparks, R.S.J., 2006. The genesis of intermediate and silicicmagmas in deep crustal hot zones. J. Petrol. 47, 505–539.

Arevalo, R.J., McDonough, W.F., 2008. Tungsten geochemistry and implications for understanding the earth's interior. Earth Planet. Sci. Lett. 272, 656–665.

Audétat, A., Günther, D., Heinrich, C.A., 2000. Magmatic-hydrothermal evolution in a fractionating granite: a microchemical study of the Sn-W-F mineralized Mole Granite (Australia). Geochim. Cosmochim. Acta 64, 3373–3393.

Ballouard, C., Poujol, M., Boulvais, P., Branquet, Y., Tartese, R., Vigneresse, J.L., 2016. Nb-Ta fractionation in peraluminous granites: a marker of magmatic-hydrothermal transition. Geology 3, 231–234.

Batchelor, R.A., Bowden, V.P., 1985. Petrogenetic interpretation of granitoids rock series using multicationic parameters. Chem. Geol. 48, 43–55.

Bau, M., 1996. Controls on the fractionation of isovalent trace elements in magmatic and aqueous systems: evidence from Y/Ho, Zr/Hf, and lanthanide tetrad effect. Contrib. Mineral. Petrol. 123, 323–333.

Beddoestephens, B., Fortey, N.J., 1981. Columbite from the Carrock Fell tungsten deposit. Mineral. Mag. 44, 217–223.

Belousova, E.A., Griffin, W.L., O'Reilly, S.Y., Fisher, N.I., 2002. Igneous zircon: trace element composition as an indicator of source rock type. Contrib. Mineral. Petrol. 143, 602–622.

Bouvier, A., Vervoort, J.D., Patchett, P.J., 2008. The Lu-Hf and Sm-Nd isotopic composition of CHUR, constraints from unequilibrated chondrites and implications for the bulk composition of terrestrial planets. Earth Planet. Sci. Lett. 273, 48–57.

Campbell, I.H., Stepanov, A.S., Liang, H.Y., Allen, C.M., Norman, M.D., Zhang, Y.Q., Xie, Y.W., 2014. The origin of shoshonites: new insights from the Tertiary high-potassium intrusions of eastern Tibet. Contrib. Mineral. Petrol. 167, 983.

Cao, H.H., Xu, W.L., Pei, F.P., Wang, Z.W., Wang, F., Wang, Z.J., 2013. Zircon U-Pb geochronology and petrogenesis of the late Paleozoic-early Mesozoic intrusive rocks in the eastern segment of the northern margin of the North China Block. Lithos 170–171, 191–207.

Cao, J.Y., Wu, Q.H., Yang, X.Y., Deng, X.T., Li, H., Kong, H., Xi, X.S., 2020. Geochemical factors revealing the differences between the Xitian and Dengfuxian composite plutons, middle Qin-Hang Belt: Implications to the W-Sn mineralization. Ore Geol. Rev. 118, 103353.

Cao, J.Y., Wu, Q.H., Yang, X.Y., Kong, H., Li, H., Xi, X.S., Huang, Q.F., Liu, B., 2018a. Geochronology and genesis of the Xitian W-Sn polymetallic deposit in Eastern Hunan Province, South China: evidence from zircon U-Pb and muscovite Ar-Ar dating, petrochemistry, and wolframite Sr-Nd-Pb isotopes. Minerals 8, 23.

Cao, J.Y., Yang, X.Y., Du, J.G., Wu, Q.H., Kong, H., Li, H., Wan, Q., Xi, X.S., Gong, Y.S., Zhao, H.R., 2018b. Formation and geodynamic implication of the early Yanshanian granites associated with W-Sn mineralization in the Nanling range, South China: an overview. Int. Geol. Rev. 60, 1744–1771.

Carr, P.A., Mercadier, J., Harlaux, M., Romer, R.L., Moreira, E., Legros, H., Cuney, M., Marignac, C., Cauzid, J., Salsi, L., Lecomte, A., Rouer, O., Peiffert, C., 2021. U/Pb geochronology of wolframite by LA-ICP-MS; mineralogical constraints, analytical procedures, data interpretation, and comparison with ID-TIMS. Chem. Geol. 584, 120511.

Černý, P., Ercit, T.S., 1989. Mineralogy of niobium and tantalum: Crystal chemical relationships, paragenetic aspects and their economic implications. In: Möller, P., Černý, P., Saupé, F. (Eds.), Lanthanides, Tantalum and Niobium. Springer-Verlag, Berlin and Heidelberg.

Černý, P., Novák, M., Chapman, R., Ferreira, K.J., 2007. Subsolidus behavior of niobian rutile from the Písek region, Czech Republic: a model for exsolution in W-and $Fe2+ \gg Fe3+$-rich phases. J. Geosci. 52, 143–159.

Chappell, B.W., 1999. Aluminium saturation in I- and S-type granites and the characterization of fractionated haplogranites. Lithos 46, 535–551.

Chappell, B.W., White, A.J.R., 1992. I-and S-type granites in the Lachlan Fold Belt. Earth Environ. Sci. Trans. R. Soc. Edinb. 83, 1–26.

Chappell, B.W., White, A.J.R., 2001. Two constrasting granite types: 25 years later. Aust. J. Earth Sci. 48, 489–499.

Che, X.D., Linnen, R.L., Wang, R.C., Aseri, A., Thibault, Y., 2013. Tungsten solubility in evolved granitic melts: an evaluation of magmatic wolframite. Geochim. Cosmochim. Acta 106, 84–98.

Chen, B., Jahn, B.M., Tian, W., 2009. Evolution of the Solonker suture zone: constraints from zircon U-Pb ages, Hf isotopic ratios and whole-rock Nd-Sr isotope compositions of subduction- and collision-related magmas and forearc sediments. J. Asian Earth Sci. 34, 245–257.

Chen, P.W., Liu, B., Long, Z., Zhou, L.L., Fu, Y., Zeng, Q.D., 2022. Ore genesis of the Sadaigoumen porphyry Mo deposit, North China Craton: Constraints from pyrite trace element and lead isotope analyses. Ore Geol. Rev. 142, 104698.

Chen, P.W., Zeng, Q.D., Zhou, T.C., 2020. Petrogenesis and Mo prospecting significance of Sadaigoumen granites on the northern margin of the North China Craton. J. Geochem. Explor. 214, 106536.

Chen, X., Liu, J.J., Zhang, D.H., Zhang, Q.B., Yang, S.S., Li, Y.C., Cao, Q., 2017. Re-Os dating of molybdenites and S-Pb isotopic characteristics of the Cuihongshan iron polymetallic depositHeilongjiang Province. Acta Petrologica Sinica. 33, 529–544 (in Chinese with English abstract).

Chew, D.M., Sylvester, P.J., Tubrett, M.N., 2011. U-Pb and Th-Pb dating of apatite by LA-ICPMS. Chem. Geol. 280, 200–216.

Claiborne, L.L., Miller, C.F., Walker, B.A., Wooden, J.L., Mazdab, F.K., Bea, F., 2006. Tracking magmatic processes through Zr/Hf ratios in rocks and Hf and Ti zoning in zircons: an example from the Spirit Mountain batholithNevada. Mineralogical Magazine 70, 517–543.

Collins, W.J., Huang, H.Q., Jiang, X.Y., 2016. Water-fluxed crustal melting produces Cordilleran batholiths. Geology 44, 143–146.

Condie, K.C., 1976. Plate Tectonics and Crustal Evolution, second ed. Pergamon Press, New York.

Deering, C.D., Bachmann, O., 2010. Trace element indicators of crystal accumulation in silicic igneous rocks. Earth Planet. Sci. Lett. 297, 324–331.

Deng, X.D., Luo, T., Li, J.W., Hu, Z.C., 2019. Direct dating of hydrothermal tungsten mineralization using in situ wolframite U-Pb chronology by laser ablation ICP-MS. Chem. Geol. 515, 94–104.

Dewaele, S., Clercq, F.D., Hulsbosch, N., Piessens, K., Boyce, A., Burgess, R., Muchez, P., 2016. Genesis of the vein-type tungsten mineralization at Nyakabingo (Rwanda) in the Karagwe-Ankole beltCentral Africa. Mineralium Deposita. 51, 283–307.

Dostal, J., Chatterjee, A.K., 2000. Contrasting behavior of Nb/Ta and Zr/Hf ratios in a peraluminous granitic pluton (Nova Scotia, Canada). Chem. Geol. 163, 207–218.

Dostal, J., Kontak, D.J., Gerel, O., Gregory, S.J., Fayek, M., 2015. Cretaceous ongonites (topaz-bearing albite-rich microleucogranites) from Ongon Khairkhan, Central Mongolia: products of extreme magmatic fractionation and pervasive metasomatic fluid: rock interaction. Lithos 236–237, 173–189.

EI Bouseily, A.M., EI Sokkary, A.A., 1975. The relation between Rb, Ba and Sr in granitic rocks. Chemical Geology 16, 207–219.

Eizenhöfer, P.R., Zhao, G.C., Zhang, J., Sun, M., 2014. Final closure of the Paleo-Asian Ocean along the Solonker suture zone: constraints from geochronological and geochemical data of Permian volcanic and sedimentary rocks. Tectonics 33, 441–463.

Fei, X.H., Zhang, Z.C., Cheng, Z.G., Santosh, M., Jin, Z.L., Wen, B.B., Li, Z.X., Xu, L.J., 2018. Highly differentiated magmas linked with polymetallic mineralization: a case study from the Cuihongshan granitic intrusions, Lesser Xing'an Range, NE China. Lithos 302–303, 158–177.

Feng, Y.Y., Fu, W., Feng, Z.H., Yang, J.W., Li, Z.Y., Le, X.W., Li, S.S., Feng, M., Wang, C. Z., Xu, J.F., 2021. Petrogenesis and metallogenesis of an extraordinary deeply hidden granite pluton overlain by W-Zn-Pb-Ag-mineralized roof: example from Xidamingshan districtSouth China. Ore Geology Reviews 130, 103932.

Feng, Z.Q., Liu, Y.J., Li, L., Jin, W., Jiang, L.W., Li, W.M., Wen, Q.B., Zhao, Y.L., 2019. Geochemical and geochronological constraints on the tectonic setting of the Xinlin ophiolite, northern Great Xing'an Range, NE China. Lithos 326–327, 213–229.

Fogliata, A.S., Baez, M.A., Hagemann, S.G., Santos, J.O., Sardi, F., 2012. Post-orogenic, Carboniferous granite-hosted Sn-W mineralization in the Sierras Pampeanas OrogenNorthwestern Argentina. Ore Geology Reviews. 45, 16–32.

Gan, G.L., Chen, Z.X., 1992. Compositional characteristics of wolframite in tin deposits, DupanglingGuangxi. Chinese Journal of Geochemistry 11, 156–167.

Gao, X., Zhou, Z., Breiter, K., Ouyang, H., Liu, J., 2019. Ore-formation mechanism of the Weilasituo tin–polymetallic deposit, NE China: constraints from bulk-rock and mica chemistry, He–Ar isotopes, and Re–Os dating. Ore Geol. Rev. 109, 163–183.

Ghaderi, M., Palin, J.M., Campbell, I.H., Sylvester, P.J., 1999. Rare earth element systematics in scheelite from hydrothermal gold deposits in the Kalgoorlie-Norseman regionWestern Australia. Economic Geology 94, 423–437.

Gibert, F., Moine, B., Schott, J., Dandurand, J.L., 1992. Modeling of the transport and deposition of tungsten in the scheelite-bearing calc-silicate gneisses of the Montagne NoireFrance. Contributions To Mineralogy and Petrology 112, 371–384.

Goldmann, S., Melcher, F., Gabler, H.E., Dewaele, S., Clercq, F.D., Muchez, P., 2013. Mineralogy and trace element chemistry of ferberite/reinite from tungsten deposits in Central Rwanda. Minerals 3, 121–144.

Gou, J., Sun, D.Y., Ren, Y.S., Liu, Y.J., Zhang, S.Y., Fu, C.L., Wang, T.H., Wu, P.F., Liu, X. M., 2013. Petrogenesis and geodynamic setting of Neoproterozoic and late Paleozoic magmatism in the Manzhouli-Erguna area of Inner Mongolia, China: geochronological, geochemical and Hf isotopic evidence. J. Asian Earth Sci. 67–68, 114–137.

Green, T.H., 1995. Significance of Nb/Ta as an indicator of geochemical processes in the crust-mantle system. Chem. Geol. 120, 347–359.

Griffin, W.L., Wang, X., Jackson, S.E., Pearson, S.E., O'Reilly, S.Y., Xu, X.S., Zhou, X.M., 2002. Zircon chemistry and magma genesis, SE China: in-situ analysis of Hf isotopes, Tonglu and Pingtan igneous complexes. Lithos 61, 237–269.

Guo, F., Li, H., Fan, W.M., Li, J., Zhao, L., Huang, M., Xu, W., 2015. Early Jurassic subduction of the Paleo-Pacific Ocean in NE China: petrologic and geochemical evidence from the Tumen mafic intrusive complex. Lithos 224–225, 46–60.

Guo, Z.J., Li, J.W., Huang, G.J., Guan, J.D., Dong, X.Z., Tian, J., Yang, Y.C., She, H.Q., Xiang, A.P., Kang, Y.J., 2014. Sr-Nd-Pb-Hf isotopic characteristics of ore-bearing granites in the Honghuaerji scheelite depositInner Mongolia. Geology in China 41, 1226–1241 (in Chinese with English abstract).

Guo, Z.J., Li, J.W., Xu, X.Y., Song, Z.Y., Dong, X.Z., Tian, J., Yang, Y.C., She, H.Q., Xiang, A.P., Kang, Y.J., 2016. Sm-Nd dating and REE Composition of scheelite for the Honghuaerji scheelite deposit, Inner Mongolia, Northeast China. Lithos 261, 307–321.

Han, J., Zhou, J.B., Wang, B., Cao, J.L., 2015. The final collision of the CAOB: constraint from the zircon U-Pb dating of the Linxi FormationInner Mongolia. Geoscience Frontiers 6, 211–225.
Hao, Y.J., Ren, Y.S., Zhao, H.L., Zou, X.T., Chen, C., Hou, Z.S., Qu, W.J., 2013. Re-Os isotopic dating of the molybdenite from the Cuihongshan W-Mo polymetallic deposit in Heilongjiang Province and its geological significance. J. Jilin Univ. (Earth Sci. Ed.) 43, 1840–1850 (in Chinese with English abstract).
Harlaux, M., Mercadier, J., Marignac, C., Peiffert, C., Cloquet, C., Cuney, M., 2018. Tracing metal sources in peribatholitic hydrothermal W deposits based on the chemical composition of wolframite: the example of the Variscan French Massif Central. Chem. Geol. 479, 58–85.
Harris, N.B., Pearce, J.A., Tindle, A.G., 1986. Geochemical Characteristics of Collision-zone Magmatism. Special Publications, London.
Hofmann, A.W., Jochum, K.P., Seufert, M., White, W.M., 1986. Nb and Pb in oceanic basalts: new constraints on mantle evolution. Earth Planet. Sci. Lett. 90, 33–45.
Hu, P., Nie, F.J., He, Y., Liu, Y., 2006. A peraluminous granite with positive εNd(t) values: the Shamai pluton in Inner Mongolia, Northeast China. Acta Petrol. Sin. 22, 2781–2790 (in Chinese with English abstract).
Hu, X.L., Ding, Z.J., He, M.C., Yao, S.Z., Zhu, B.P., Shen, J., Chen, B., 2014. Two epochs of magmatism and metallogeny in the Cuihongshan Fe-polymetallic deposit, Heilongjiang Province, NE China: constrains from U-Pb and Re–Os geochronology and Lu–Hf isotopes. J. Geochem. Explor. 143, 116–126.
Huang, L.C., Jiang, S.Y., 2014. Highly fractionated S-type granites from the giant Dahutang tungsten deposit in Jiangnan orogen, Southeast China: geochronology, petrogenesis and their relationship with W-mineralization. Lithos 202–203, 207–226.
Hulsbosch, N., Boiron, M.C., Dewaele, S., Muchez, P., 2016. Fluid fractionation of tungsten during granite-pegmatite differentiation and the metal source of peribatholitic W quartz veins: evidence from the Karagwe-Ankole belt (Rwanda). Geochim. Cosmochim. Acta 175, 299–318.
IMBGMR (Inner Mongolian Bureau of Geology Mineral Resources), 1991. In: Regional Geology of Inner Mongolia. Geological Publishing House, Beijing, pp. 1–725 (in Chinese).
Jiang, H., Jiang, S.Y., Li, W.Q., Zhao, K.D., Peng, N.J., 2018. Highly fractionated Jurassic I-type granites and related tungsten mineralization in the Shirenzhang deposit, northern Guangdong, South China: evidence from cassiterite and zircon U-Pb ages, geochemistry and Sr-Nd-Pb-Hf isotopes. Lithos 312–313, 186–203.
Jiang, S.H., Bagas, L., Hu, P., Han, N., Chen, C.L., Liu, Y., Kang, H., 2016. Zircon U-Pb ages and Sr–Nd–Hf isotopes of the highly fractionated granite with tetrad REE patterns in the Shamai tungsten deposit in eastern Inner Mongolia, China: implications for the timing of mineralization and ore genesis. Lithos 261, 322–339.
Jiang, S.H., Chen, C.L., Bagas, L., Liu, Y., Han, N., Kang, H., Wang, Z.H., 2017. Two mineralization events in the Baiyinnuoer Zn-Pb deposit in Inner Mongolia China: evidence from field observations, S-Pb isotopic compositions and U-Pb zircon ages. J. Asian Earth Sci. 144, 339–367.
Jiang, S.H., Nie, F.J., Liu, Y.F., Huo, W.R., Bai, D.M., Liu, Y., Liang, Q.L., 2011. Geochronology of intrusive rocks occurring in and around the Mengentaolegai silver-polymetallic depositInner Mongolia. Journal of Jilin University (Earth Science Edition) 41, 1756–1769 (in Chinese with English abstract).
Keay, S., Collins, W.J., McCulloch, M.T., 1997. A three-component Sr-Nd isotopic mixing model for granitoid genesis, Lachlan fold belt, eastern Australia. Geology 25, 307–310.
Kemp, A.I.S., Hawkesworth, C.J., Foster, G.L., Paterson, B.A., Woodhead, J.D., Hergt, J. M., Gray, C.M., Whitehouse, M.J., 2007. Magmatic and crustal differentiation history of granitic rocks from Hf-O isotopes in zircon. Science 315, 980–983.
Keppler, H., Wyllie, P.J., 1991. Partitioning of Cu, Sn, Mo, W, U, and Th between melt and aqueous fluid in the systems haplogranite-H2O-HCl and haplogranite-H2O-HF. Contrib. Mineral. Petrol. 109, 139–150.
Korges, M., Weis, P., Lüders, V., Laurent, O., 2018. Depressurization and boiling of a single magmatic fluid as a mechanism for tin-tungsten deposit formation. Geology 46, 75–78.
Lecumberri-Sanchez, P., Vieira, R., Heinrich, C.A., Pinto, F., Wälle, M., 2017. Fluid-rock interaction is decisive for the formation of tungsten deposits. Geology 45, 579–582.
Legros, H., Richard, A., Tarantola, A., Kouzmanov, K., Mercadier, J., Vennemann, T., Marignac, C., Cuney, M., Wang, R.C., Charles, N., Bailly, L., 2019. Multiple fluids involved in granite-related W-Sn deposits from the world-class Jiangxi province (China). Chem. Geol. 508, 92–115.
Lehmann, B., 1987. Tin granites, geochemical heritage, magmatic differentiation. Geol. Rundsch. 76, 177–185.
Lehmann, B., Ishihara, S., Michel, H., Miller, J., Rapela, C., Sanchez, A., Tistl, M., Winkelmann, L., 1990. The Bolivian tin province and regional tin distribution in the Central Andes: a reassessment. Econ. Geol. 85, 1044–1058.
Li, J., Huang, X.L., Fu, Q., Li, W.X., 2021a. Tungsten mineralization during the evolution of a magmatic-hydrothermal system: mineralogical evidence from the Xihuashan rare-metal granite in South China. Am. Mineral. 106, 443–460.
Li, J.J., Fu, C., Tang, W.L., Li, H.M., Lin, Y.X., Zhang, T., Wang, S.G., Zhao, Z.L., Dang, Z. C., Zhao, L.J., 2016a. The metallogenic age of the Shamai wolframite deposit in Dong Ujimqin BannerInner Mongolia. Geological Bulletin of China. 35, 524–530 (in Chinese with English abstract).
Li, J.J., Zhou, Y., Dang, Z.C., Zhao, Z.L., Li, C., Qu, W.J., Cao, Z.C., Yang, G.J., Fu, C., Tang, W.L., 2016b. Re-Os isotopic dating of molybdenites from the Sansheng W-Mo deposit in Huada County, Inner Mongolia, and its geological significance. Geol. Bull. China 35, 531–536 (in Chinese with English abstract).
Li, J.Y., Gao, L.M., Sun, G.H., Li, Y.P., Wang, Y.B., 2007. Shuangjingzi Middle Triassic syn-collisional crust-derived granite in the East Inner Mongolia and its constraint on the timing of collision between Siberian and Sino-korean paleo-plates. Acta Petrol. Sin. 23, 565–582 (in Chinese with English abstract).
Li, P.W., Gao, R., Guan, Y., Li, Q.S., 2006. Palaeomagnetic constraints on the final closure time of Solonker-Linxi suture. J. Jilin Univ. (Earth Sci. Ed.) 36, 744–758 (in Chinese with English abstract).
Li, S., Wilde, S.A., He, Z.J., Jiang, X.J., Liu, R.Y., Zhao, L., 2014a. Triassic sedimentation and postaccretionary crustal evolution along the Solonker suture zone in Inner MongoliaChina. Tectonics 33, 960–981.
Li, W.S., Ni, P., Pan, J.Y., Fan, M.S., Chen, L.L., Zhang, D., Wu, X.W., Gao, Y., 2021. Constraints on the timing and genetic link of scheelite- and wolframite-bearing quartz veins in the chuankou W ore field, South China. Ore Geol. Rev. 133, 104122.
Li, W.S., Ni, P., Pan, J.Y., Wang, G.G., Chen, L.L., Yang, Y.L., Ding, J.Y., 2018. Fluid inclusion characteristics as an indicator for tungsten mineralization in the Mesozoic Yaogangxian tungsten deposit, central Nanling district, South China. J. Geochem. Explor. 192, 1–17.
Li, W.S., Ni, P., Wang, G.G., Yang, Y.L., Pan, J.Y., Wang, X.L., Chen, L.L., Fan, M.S., 2020. A possible linkage between highly fractionated granitoids and associated W-mineralization in the Mesozoic Yaogangxian granitic intrusion, Nanling region, South China. J. Asian Earth Sci. 193, 104314.
Li, Y.L., Zhou, H.W., Brouwer, F.M., Xiao, W.J., Wijbrans, J.R., Zhao, J.H., Zhong, Z.Q., Liu, H.F., 2014b. Nature and timing of the Solonker suture of the Central Asian Orogenic Belt: insights from geochronology and geochemistry of basic intrusions in the Xilin Gol complex, Inner MongoliaChina. International Journal of Earth Sciences 103, 41–60.
Li, Y.S., Yu, X.F., Mi, K.F., Carranza, E.J.M., Liu, J.J., Jia, W.B., He, S., 2019. Deposit geology, geochronology and geochemistry of the Gongpengzi skarn Cu-Zn-W polymetallic depositNE China. Ore Geology Reviews 109, 465–481.
Liegeois, G.P., 1998. Preface-some words on the post-collisional magmatism. Lithos 45, 15–17.
Linnen, R.L., Keppler, H., 1997. Columbite solubility in granitic melts: consequences for the enrichment and fractionation of Nb and Ta in the Earth's crust. Contrib. Mineral. Petrol. 128, 213–227.
Linnen, R.L., Keppler, H., 2002. Melt composition control of Zr/Hf fractionation in magmatic processes. Geochim. Cosmochim. Acta 66, 3293–3301.
Linnen, R.L., Williams-Jones, A.E., 1995. Genesis of a magmatic metamorphic hydrothermal system; the Sn-W polymetallic deposits at PilokThailand. Economic Geology 90, 1921–1935.
Litvinovsky, B.A., Jahn, B.M., Eyal, M., 2015. Mantle-derived sources of syenites from the A-type igneous suites-new approach to the provenance of alkaline silicic magmas. Lithos 232, 242–265.
Liu, C.H., Nie, F.J., 2015. Permian magmatic sequences of the Bilihe gold deposit in Central Inner Mongolia, China: petrogenesis and tectonic significance. Lithos 231, 35–52.
Liu, Y.F., Jiang, S.H., Bagas, L., 2016. The genesis of metal zonation in the Weilasituo and Bairendaba Ag–Zn–Pb–Cu–(Sn–W) deposits in the shallow part of a porphyry Sn–W–Rb system, Inner Mongolia,China. Ore Geology Reviews 75, 150–173.
Liu, Y.J., Li, W.M., Feng, Z.Q., Wen, Q.B., Neubauer, F., Liang, C.Y., 2017. A review of the Paleozoic tectonics in the eastern part of Central Asian Orogenic Belt. Gondwana Res. 43, 123–148.
Liu, Y.S., Gao, S., Hu, Z.C., Gao, C.G., Zong, K.Q., Wang, D.B., 2010a. Continental and oceanic crust recycling-induced melt-peridotite interactions in the Trans-North China Orogen: U-Pb dating, Hf isotopes and trace elements in zircons from mantle xenoliths. J. Petrol. 51, 537–571.
Liu, Y.S., Hu, Z.C., Gao, S., Günther, D., Xu, J., Gao, C.G., Chen, H.H., 2008. In situ analysis of major and trace elements of anhydrous minerals by LA-ICP-MS without applying an internal standard. Chem. Geol. 257, 34–43.
Liu, Y.S., Hu, Z.C., Zong, K.Q., Gao, C.G., Gao, S., Xu, J., Chen, H.H., 2010b. Reappraisement and refinement of zircon U-Pb isotope and trace element analyses by LA-ICP-MS. Chin. Sci. Bull. 55, 1535–1546.
Ludwig, K.R., 2003. In: User's Manual for Isoplot 3.00: A Geochronological Toolkit for Microsoft Excel, 4. Bereley Geochronology Center Special Publication, pp. 1–70.
Luo, T., Deng, X.D., Li, J.W., Hu, Z.C., Zhang, W., Liu, Y.S., Zhang, J.F., 2019. U-Pb geochronology of wolframite by laser ablation inductively coupled plasma mass spectrometry. J. Anal. At. Spectrom. 34, 1439–1446.
Ma, X.H., Zhu, W.P., Zhou, Z.H., Qiao, S.L., 2017. Transformation from Paleo-Asian Ocean closure to Paleo-Pacific subduction: new constraints from granitoids in the eastern Jilin-Heilongjiang Belt, NE China. J. Asian Earth Sci. 144, 261–286.
Maniar, P.D., Piccoli, P.M., 1989. Tectonic discrimination of granitoids. Geol. Soc. Am. Bull. 101, 635–643.
Manya, S., Maboko, M.A.H., 2016. Generation of Palaeoproterozoic tonalites and associated high-K granites in southwestern Tanzania by partial melting of underplated mafic crust in an intracontinental setting: constraints from geochemical and isotopic data. Lithos 260, 120–133.
Mao, A.Q., Sun, D.Y., Gou, J., Yang, D.G., Zheng, H., 2020. Late Palaeozoic-early Mesozoic southward subduction of the Mongol-Okhotsk oceanic slab: geochronological, geochemical, and Hf isotopic evidence from intrusive rocks in the Erguna Massif (NE China). Int. Geol. Rev. https://doi.org/10.1080/00206814.00202020.01758968.
Mao, J.W., Cheng, Y.B., Chen, M.H., Franco, P., 2013. Major types and time–space distribution of Mesozoic ore deposits in South China and their geodynamic settings. Mineral. Deposita 48, 267–294.
McDonough, W.F., Sun, S.S., 1995. The composition of the earth. Chem. Geol. 120, 223–253.
Middlemost, E.A.K., 1994. Naming materials in the magma/igneous rock system. Earth Sci. Rev. 37, 215–224.

Miller, C.F., Mittlefehldt, D.W., 1982. Depletion of light rare-earth elements in felsic magmas. Geology 10, 129–133.
Miller, C.F., Mittlefehldt, D.W., 1984. Extreme fractionation in felsic magma chambers: a product of liquid-state diffusion or fractional crystallization? Earth Planet. Sci. Lett. 151–158.
Mushkin, A., Navon, O., Halicz, L., Hartmann, G., Stein, M., 2003. The petrogenesis of A-type magmas from the Amram Massif, southern Israel. J. Petrol. 44, 815–832.
Ni, P., Li, W.S., Pan, J.Y., 2020. Ore-forming fluid and metallogenic mechanism of wolframite-quartz vein type tungsten deposits in south China. Acta Geol. Sin. (Eng. Ed.) 94, 1774–1796.
Ouyang, H.G., Mao, J.W., Santosh, M., Zhou, J., Zhou, Z.H., Wu, Y., Hou, L., 2013. Geodynamic setting of Mesozoic magmatism in NE China and surrounding regions: perspectives from spatio-temporal distribution patterns of ore deposits. J. Asian Earth Sci. 78, 222–236.
Ouyang, H.G., Mao, J.W., Zhou, Z.H., Su, H.M., 2015. Late Mesozoic metallogeny and intracontinental magmatism, southern Great Xing'an Range, northeastern China. Gondwana Res. 27, 1153–1172.
Pan, H.R., 2010. Check Report on Utilization Status of Tungsten Resources in Tantou Mountain, Kangbao County, Hebei Province (in Chinese).
Pan, J.Y., Ni, P., Wang, R.C., 2019. Comparison of fluid processes in coexisting wolframite and quartz from a giant vein-type tungsten deposit, South China: insights from detailed petrography and LA-ICP-MS analysis of fluid inclusions. Am. Mineral. 104, 1092–1116.
Pearce, J.A., Harris, N.B.W., Tindle, A.G., 1984. Trace element discrimination diagrams for the tectonic interpretation of granitic rocks. J. Petrol. 25, 956–983.
Peccerillo, A., Taylor, S.R., 1976. Geochemistry of eocene calc-alkaline volcanic rocks form the Kastamonu area, Northern Turkey. Contrib. Mineral. Petrol. 58, 63–81.
Peng, N.L., Xi, X.S., Kong, H., Chen, Z.F., Wang, G., 2015. Re-Os isotopic dating of molybdenites from the Shazigou W-Mo polymetallic deposit, Inner Mongolia and its geological implications. Geol. Explor. 51, 838–848 (in Chinese with English abstract).
Peng, P., 2015. Precambrian mafic dyke swarms in the North China Craton and their geological implications. Sci. China Earth Sci. 58, 649–675.
Pitcher, W.S., 1987. Granites and yet more granites forty years on. Geol. Rundsch. 76, 51–79.
Plank, T., 2005. Constraints from thorium/lanthanum on sediment recyeling at subduction zones and the evolution of the continents. J. Petrol. 46, 921–944.
Polya, D.A., 1988. Compositional variation in wolframites from the Barroca Grande mine, Portugal: evidence for fault-controlled ore formation. Mineral. Mag. 52, 497–503.
Qin, H.F., Li, Y.F., Huang, C., Cai, S.H., Ren, S.M., 2013. Palaeomagnetic investigation of Permain sandstone in Taohaiyingzi area of Inner Mongolia and its tectonic significance. Geol. Bull. China 32, 388–398 (in Chinese with English abstract).
Raimbault, L., Baumer, A., Dubru, M., Benkerrou, C., Croze, V., Zahm, A., 1993. REE fractionation between scheelite and apatite in hydrothermal conditions. Am. Mineral. 78, 1275–1285.
Refy, F.G., 1997. Direct evolution of W-rich brines from crystallizing melt within the Mariktikan granite pluton, west Transbaikalia. Mineral. Deposita 32, 475–490.
Roberts, N.M., Rasbury, E.T., Parrish, R.R., Smith, C.J., Horstwood, M.S., Condon, D.J., 2017. A calcite reference material for LA-ICP-MS U-Pb geochronology. Geochem. Geophys. Geosyst. 18, 2807–2814.
Romer, R.L., Kroner, U., 2016. Phanerozoic tin and tungsten mineralization—tectonic controls on the distribution of enriched protoliths and heat sources for crustal melting. Gondwana Res. 31, 60–95.
Romer, R.L., Meixner, A., Förster, H.J., 2014. Lithium and boron in late-orogenic granites – Isotopic fingerprints for the source of crustal melts? Geochim. Cosmochim. Acta 131, 98–114.
Rudnick, R.L., Gao, S., 2003. 3.01−Composition of the continental crust. In: Treatise on Geochemistry, 3, pp. 1–64.
Schaller, T., Dingwell, D.B., Keppler, H., Knöller, W., Merwin, L., Sebald, A., 1992. Fluorine in silicate glasses: a multinuclear nuclear magnetic resonance study. Geochim. Cosmochim. Acta 56, 701–707.
Sengör, A.M.C., Natal'in, B.A., Burtman, V.S., 1993. Evolution of the Altaid tectonic collage and Paleozoic crustal growth in Eurasia. Nature 364, 299–307.
Shang, Q.H., 2004. Occurrences of Permian ra-diolarians in central and eastern Nei Mongol (Inner Mongolia) and their geological significance to the Northern China Orogen. Chin. Sci. Bull. 49, 2613–2619.
Shang, Q.Q., Ren, Y.S., Chen, C., Zhao, H.L., Li, C.H., 2017. Metallogenic age and ore-forming material source of Yangjin'gou gold deposit in eastern Yanbian region. Gold 38, 7–12 (in Chinese with English abstract).
Shannon, R.D., 1976. Revised effective ionic radii and systematic studies of interatomic distances in halides and chalcogenides. Acta Crystallogr. 32, 751–767.
Shao, J., Li, X.R., Yang, H.Z., 2011. Zircon SHRIMP U-Pb dating of granite in the Cuihongshan polymetallic deposit and its geological implications. Acta Geosci. Sin. 32, 163–170 (in Chinese with English abstract).
Shi, Y.R., Liu, D.Y., Miao, L.C., Zhang, F.Q., Jian, P., Zhang, W., Hou, K.J., Xu, J.Y., 2010. Devonian A-type granitic magmatism on the norhern margin of the North China Craton: SHRIMP U-Pb zircon dating and Hf isotopes of the Hongshan granite at Chifeng, Inner MongoliaChina. Gondwana Research 17, 632–641.
Signorelli, S., Carroll, M.R., 2000. Solubility and fluid-melt partitioning of Cl in hydrous phonolitic melts. Geochim. Cosmochim. Acta 64, 2851–2862.
Singh, S.K., Singh, S., 2001. Geochemistry and tungsten metallogeny of the Balda granite, Rajasthan. India. Gondwana Research 4, 487–495.
Söderlund, U., Patchett, P.J., Vervoort, J.D., Isachsen, C.E., 2004. The 176Lu decay constant determined by Lu-Hf and U-Pb isotope systematics of Precambrian mafic intrusions. Earth Planet. Sci. Lett. 219, 311–324.
Stein, H.J., 2014. Dating and tracing the history of ore formation. In: Turekian, K.K., Holland, H.D., Scott, S.D. (Eds.), Treatise in Geochemistry, 2nd ed., Vol. 12. Elsevier-Pergamon, Oxford.
Steiner, B.M., 2019. W and Li-Cs-Ta geochemical signatures in I-type granites−a case study from the Vosges Mountains, NE France. J. Geochem. Explor. 197, 238–250.
Sun, D.Y., Wu, F.Y., Zhang, Y.B., Gao, S., Singh, S.K., Singh, S., 2004. The final closing time of the west Lamulun River-Changchun-Yanji plate suture zone: evidence from the Dayushan granitic plutonJilin Province. Journal of Jilin University (Earth Science Edition) 34, 174–181 (in Chinese with English abstract).
Sun, S.S., McDonough, W.F., 1989. Chemical and isotopic systematics of oceanic basalts: implications for mantle composition and processes. In: Saunders, A.D., Norry, M.J. (Eds.), Magmatism in the Ocean Basins. Special Publications, London.
Tang, Y.W., Cui, K., Zheng, Z., Gao, J.F., Han, J.J., Yang, J.H., Liu, L., 2020. LA-ICP-MS U Pb geochronology of wolframite by combining NIST series and common lead-bearing MTM as the primary reference material: implications for metallogenesis of South China. Gondwana Res. 83, 217–231.
Tang, Y.W., Gao, J.F., Lan, T.G., Cui, K., Han, J.J., Zhang, X., Chen, Y.W., Chen, Y.H., 2021. In situ low-U garnet U-Pb dating by LA-SF-ICP-MS and its application in constraining the origin of Anji skarn system combined with Ar-Ar dating and Pb isotopes. Ore Geol. Rev. 130, 103970.
Taylor, S.R., McLennan, S.M., 1995. The geochemical evolution of the continental crust. Rev. Geophys. 33, 241–265.
Thomas, R., Förster, H.J., Rickers, K., Webster, J.D., 2005. Formation of extremely F-rich hydrous melt fractions and hydrothermal fluids during differentiation of highly evolved tin-granite magmas: a melt/fluid-inclusion study. Contrib. Mineral. Petrol. 148, 582–601.
Tindle, A.G., Breaks, F.W., Webb, P.C., 1998. Wodginite-group minerals from the separation rapids rare-element granitic pegmatite group, northwestern Ontario. Can. Mineral. 36, 637–658.
Tindle, A.G., Webb, P.C., 1989. Niobian wolframite from Glen Gairn in the Eastern Highlands of Scotland: a microprobe investigation. Geochim. Cosmochim. Acta 53, 1921–1935.
Turner, S.P., Foden, J.D., Morrison, R.S., 1992. Derivation of some A-type magmas by fractionation of basaltic magma: an example from the Padthaway Ridge, South Australia. Lithos 28, 151–179.
Vallance, J., Cathelineau, M., Marignac, C., Boiron, M.C., Fourcade, S., Martineau, F., Fabre, C., 2001. Microfracturing and fluid mixing in granites: W-(Sn) ore deposition at Vaulry (NW French Massif Central). Tectonophysics 336, 43–61.
Vindel, E., Lopez, J.A., Boiron, M.C., Cathelineau, M., Prieto, A.C., 1995. P-V-T-X-fo2 evolution from wolframite to sulphide depositional stages in intragranitic W-veins. An example from the Spanish Central System. Eur. J. Mineral. 7, 675–688.
Wan, L., Lu, C.D., Zeng, Z.X., Mohammed, A.S., Liu, Z.H., Dai, Q.Q., Chen, K.L., 2019. Nature and significance of the late Mesozoic granitoids in the southern Great Xing'an range, eastern Central Asian Orogenic Belt. Int. Geol. Rev. 61, 584–606.
Wang, F., Bagas, L., Jiang, S., Liu, Y., 2017. Geological, geochemical, and geochronological characteristics of Weilasituo Sn-polymetal deposit, Inner MongoliaChina. Ore Geology Reviews 80, 1206–1229.
Wang, R.L., Zeng, Q.D., Zhang, Z.C., Guo, Y.P., Lu, J.H., 2020a. Fluid evolution, H-O isotope and Re-Os age of molybdenite from the Baiyinhan tungsten deposit in the Eastern Central Asian orogenic belt, NE China, and its geological significance. Minerals 10, 664.
Wang, R.L., Zeng, Q.D., Zhang, Z.C., Zhou, L.L., Qin, K.Z., 2021. Extensive mineralization in the eastern segment of the Xingmeng orogenic belt, NE China: a regional view. Ore Geol. Rev. 135, 104204.
Wang, W., Tang, J., Xu, W.L., Wang, F., 2015. Geochronology and geochemistry of early Jurassic volcanic rocks in the Erguna Massif, Northeast China: petrogenesis and implications for the tectonic evolution of the Mongol-Okhotsk suture belt. Lithos 218–219, 73–86.
Wang, Y., Tang, J.X., Wang, L.Q., Marten Huizenga, J., Santosh, M., Zheng, S.L., Hu, Y., Gao, T., 2020b. Geology, geochronology and geochemistry of the Miocene Jiaoxi quartz vein-type W deposit in the western part of the Lhasa Terrane, Tibet: implications for ore genesis. Ore Geol. Rev. 120, 103433.
Wang, Y., Xu, B., Cheng, S.D., Liao, W., Shao, J., Wang, Y., 2014. Zircon U-Pb dating of the mafic lava from Wudaoshimen, Hexigten, Inner Mongolia and its geological significance. Acta Petrol. Sin. 30, 2055–2062 (in Chinese with Englsih abstract).
Wang, Y.H., Zhang, F.F., Liu, J.J., Xue, C.J., Zhang, Z.C., 2018. Genesis of the Wurinitu W-Mo deposit, Inner Mongolia, Northeast China: constraints from geology, fluid inclusions and isotope systematics. Ore Geol. Rev. 94, 367–382.
Webster, J., Thomas, R., Förster, H.J., Seltmann, R., Tappen, C., 2004. Geochemical evolution of halogen-enriched granite magmas and mineralizing fluids of the Zinnwald tin–tungsten mining district, ErzgebirgeGermany. Mineralium Deposita 39, 452–472.
Webster, J.D., Holloway, J.R., 1988. Experimental constraints on the partitioning of Cl between topaz rhyolite melt and H2O and H2O+CO2 fluids: new implications for granitic differentiation and ore deposition. Geochim. Cosmochim. Acta 52, 2091–2105.
Wedepohl, K.H., 1995. The composition of the continental crust. Geochim. Cosmochim. Acta 59, 1217–1232.
Wei, W.F., Hu, R.Z., Bi, X.W., Peng, J.T., Su, W.C., Song, S.Q., Shi, S.H., 2012. Infrared microthermometric and stable isotopic study of fluid inclusions in wolframite at the Xihuashan tungsten deposit, Jiangxi provinceChina. Mineralium Deposita 47, 589–605.
Whalen, J.B., Currie, K.L., Chappell, B.W., 1987. A-type granites: geochemical characteristics, discrimination and petrogenesis. Contrib. Mineral. Petrol. 95, 407–419.

Wilde, S.A., 2015. Final amalgamation of the Central Asian Orogenic Belt in NE China: Paleo-Asian Ocean closure versus Paleo-Pacific plate subduction–a review of the evidence. Tectonophysics 662, 345–362.
Wood, S.A., Samson, I.M., 2000. The hydrothermal geochemistry of tungsten in granitoid environments: I. Relative solubilities of ferberite and scheelite as a function of T, P, pH, and m NaCl. Econ. Geol. 95, 143–182.
Wu, F.Y., Sun, D.Y., Ge, W.C., Zhang, Y.B., Grant, M.L., Wilde, S.A., Jahn, B.M., 2011. Geochronology of the Phanerozoic granitoids in northeastern China. J. Asian Earth Sci. 41, 1–30.
Wu, F.Y., Yang, Y.H., Xie, L.W., Yang, J.H., Xu, P., 2006. Hf isotopic compositions of the standard zircons and baddeleyites used in U-Pb geochronology. Chem. Geol. 234, 105–126.
Xiang, A.P., Chen, Y.C., Bagas, L., She, H.Q., Kang, Y.J., Yang, W.S., Li, C.J., 2016a. Molybdenite Re–Os and U-Pb zircon dating and genesis of the Dayana W-Mo deposit in eastern UjumchinInner Mongolia. Ore Geology Reviews 78, 268–280.
Xiang, A.P., Chen, Y.C., She, H.Q., Li, G.M., Li, Y.X., 2018. Chronology and geochemical characteristics of granite in Weilianhe of Inner Mongolia and its geological significance. Geol. China 45, 963–976 (in Chinese with English abstract).
Xiang, A.P., She, H.Q., Chen, Y.C., Qin, D.J., Wang, Y.J., Han, Z.G., Kang, Y.J., 2016b. Ar-Ar age of muscovite from the greisenization alteration zones of the Honghuaerji tungsten polymetallic deposit, Inner Mongolia, and its geological significance. Rock Miner. Anal. 35, 108–116 (in Chinese with English abstract).
Xiao, W.J., Santosh, M., 2014. The western Central Asian Orogenic Belt: a window to accretionary orogenesis and continental growth. Gondwana Res. 25, 1429–1444.
Xie, W., Wen, S.Q., Zhang, G.L., Tang, T.Q., 2021a. Geochronology, fluid inclusions, and isotopic characteristics of the Dongjun Pb-Zn-Ag deposit, Inner MongoliaNE China. Acta Geologica Sinica (English Edition) 95, 1611–1633.
Xie, W., Zeng, Q.D., Wang, R.L., Wu, J.J., Zhang, Z.M., Li, F.C., Zhang, Z., 2021. Spatial-temporal distribution and tectonic setting of Mesozoic W-mineralized granitoids in the Xing-Meng Orogenic Belt, NE China. International Geology Review. https://doi.org/10.1080/00206814.00202021.01961105.
Xie, W., Zeng, Q.D., Lan, T.G., Zhou, L.L., Wang, R.L., Wu, J.J., 2022a. Genetic link between the late Mesozoic granitic magmatism and W mineralization in NE China: constraints from in-situ U-Pb geochronology and geochemistry of wolframite, and whole-rocks geochemistry analyses of W-bearing granites from the Sansheng W-Mo deposit. Ore Geol. Rev. 144, 104868.
Xie, W., Zeng, Q.D., Yang, J.H., Li, R., Zhang, Z., Wang, R.L., Wu, J.J., 2022b. Petrogenesis, W metallogenic and tectonic implications of granitic intrusions in the southern Great Xing'an Rang W belt, NE China: insights from the Narenwula complex. Geol. Mag. 159, 593–627.
Xiong, Y.Q., Shao, Y.J., Cheng, Y.B., Jiang, S.Y., 2020. Discrete Jurassic and cretaceous Mineralization events at the Xiangdong W(-Sn) deposit, Nanling RangeSouth China. Economic Geology 115, 385–413.
Xiong, Y.Q., Shao, Y.J., Zhou, H.D., Wu, Q.H., Liu, J.P., Wei, H.T., Zhao, R.C., Cao, J.Y., 2017. Ore-forming mechanism of quartz-vein-type W-Sn deposits of the Xitian district in SE China: implications from the trace element analysis of wolframite and investigation of fluid inclusions. Ore Geol. Rev. 83, 152–173.
Xiong, Z.R., Li, X.N., Qi, C., Xiong, Y.Q., 2021. Geochronology of cassiterite and trace element compositions of wolframite: constraints to the ore genesis of Jiguanshi tungsten deposit, eastern Hunan Province. Acta Petrol. Sin. 37, 769–780 (in Chinese with English abstract).
Xu, B., Charvet, J., Chen, Y., Zhao, P., Shi, G.Z., 2013a. Middle Paleozoic convergent orogenic belts in western Inner Mongolia (China): framework, kinematics, geochronology and implications for tectonic evolution of the Central Asian Orogenic Belt. Gondwana Res. 23, 1342–1364.
Xu, B., Zhao, P., Wang, Y.Y., Liao, W., Luo, Z.W., Bao, Q.Z., Zhou, Y.H., 2015. The pre-Devonian tectonic framework of Xing'an-Mongolia orogenic belt (XMOB) in North China. J. Asian Earth Sci. 97, 183–196.
Xu, W.L., Pei, F.P., Wang, F., Meng, E., Ji, W.Q., Yang, D.B., Wang, W., 2013b. Spatial-temporal relationships of Mesozoic volcanic rocks in NE China: constraints on tectonic overprinting and transformations between multiple tectonic systems. J. Asian Earth Sci. 74, 167–193.
Yang, F., Sun, J.G., Wang, Y., Fu, J.Y., Na, F.C., Fan, Z.Y., Hu, Z.Z., 2019. Geology, Geochronology and Geochemistry of Weilasituo Sn-Polymetallic Deposit in Inner MongoliaChina. Minerals 9, 1–28.
Yang, M., Yang, Y.H., Wu, S.T., Romer, R.L., Che, X.D., Zhao, Z.F., Li, W.S., Yang, J.H., Wu, F.Y., Xie, L.W., Huang, C., Zhang, D., Zhang, Y., 2020. Accurate and precise in situ U-Pb isotope dating of wolframite series minerals via LA-SF-ICP-MS. J. Anal. At. Spectrom. 35, 2191–2203.
Yang, S.W., Lou, F.S., Xu, C., Feng, C.Y., Cao, S.H., Xu, D.R., Tang, Y.W., 2022. Two significant quartz-wolframite-veining mineralization events in the Jiangnan Orogen, South China: constraints from in-situ U-Pb dating of wolframite in the Dongping and Dahutang W-(Cu-Mo) deposits. Ore Geol. Rev. 141, 104598.
Yang, Z.H., Wang, J.P., Liu, J.J., Wang, S.G., Wang, Q.Y., Kang, S.G., 2012. Characteristics and its geological significance of fluid inclusions of the Wurinitu W-Mo deposit in Inner Mongolia, China. Earth Sci. - J. China Univ. Geosci. 37, 1268–1278.
Yang, Z.H., Wang, J.P., Liu, J.J., Wang, S.G., Wang, Q.Y., Kang, S.G., Zhang, J.X., Zhao, Y., 2013. Isotope geochemistry of the Wurinitu W-Mo deposit in Sunid Zuoqi, Inner MongoliaChina. Geoscience 27, 13–23 (in Chinese with English abstract).
Yang, Z.H., Wang, J.P., Liu, J.J., Wang, S.G., Wang, Q.Y., Kang, S.G., Zhang, J.X., Zhao, Y., 2016. Geochronology and geochemistry of the Wurinitu granites in Inner Mongolia and their geological implications. Geoscience 30, 528–540 (in Chinese with English abstract).
Yuan, S.D., Williams-Jones, A.E., Mao, J.W., Zhao, P.L., Yan, C., Zhang, D.L., 2018. The origin of the Zhangjialong tungsten deposit, South China: implications for W-Sn mineralization in large granite batholiths. Econ. Geol. 113, 1193–1208.
Yuan, S.D., Williams-Jones, A.E., Romer, R.L., Zhao, P.L., Mao, J.W., 2019. Protolith-Related thermal Controls on the Decoupling of Sn and W in Sn-W Metallogenic Provinces: Insights from the Nanling RegionChina. Economic Geology 114, 1005–1012.
Zajacz, Z., Halter, W.E., Pettke, T., Guillong, M., 2008. Determination of fluid/melt partition coefficients by LA-ICPMS analysis of co-existing fluid and silicate melt inclusions: controls on element partitioning. Geochim. Cosmochim. Acta 72, 2169–2197.
Zeng, Q.D., Liu, J.M., Chu, S.X., Wang, Y.B., Sun, Y., Duan, X.X., Zhou, L.L., 2012. Mesozoic molybdenum deposits in the East Xingmeng orogenic belt, Northeast China: characteristics and tectonic setting. Int. Geol. Rev. 54, 1843–1869.
Zeng, Q.D., Liu, J.M., Yu, C.M., Ye, J., Liu, H.T., 2011. Metal deposits in the Da Hinggan Mountains, NE China: styles, characteristics, and exploration potential. Int. Geol. Rev. 53, 846–878.
Zeng, Q.D., Qin, K.Z., Liu, J.M., Li, G.M., Zhai, M.G., Chu, S.X., Guo, Y.P., 2015a. Porphyry molybdenum deposits in the Tianshan-Xingmeng orogenic belt, northern China. Int. J. Earth Sci. 104, 991–1023.
Zeng, Q.D., Sun, Y., Chu, S.X., Duan, X.X., Liu, J.M., 2015b. Geochemistry and geochronology of the Dongshanwan porphyry Mo–W deposit, northeast China: Implications for the late Jurassic tectonic setting. J. Asian Earth Sci. 97, 472–485.
Zhai, M., Santosh, M., 2013. Metallogeny of the North China Craton: link with secular changes in the evolving Earth. Gondwana Res. 24, 275–297.
Zhang, H.H., Zheng, Y.J., Chen, S.W., Li, Y.F., Zhang, J., Bian, X.F., Su, F., Gong, F.H., Huang, X., 2015. Zircon U-Pb age, geochemical characteristics and geological significance of the Triassic granite in KeerginyouyizhongyiInner Mongolia. Journal of Jilin University (Earth Science Edition) 45, 417–428 (in Chinese with English abstract).
Zhang, J.H., Ge, W.C., Wu, F.Y., Wilde, S.A., Yang, J.H., Liu, X.M., 2008a. Large-scale early cretaceous volcanic events in the northern Great Xing'an Range, Northeastern China. Lithos 102, 138–157.
Zhang, Q., Zhang, R.Q., Gao, J.F., Lu, J.J., Wu, J.W., 2018. In-situ LA-ICP-MS trace element analyses of scheelite and wolframite: Constraints on the genesis of veinlet-disseminated and vein-type tungsten depositsSouth China. Ore Geology Reviews 99, 166–179.
Zhang, X.B., Wang, K.Y., Wang, C.Y., Li, W., Yu, Q., Wang, Y.C., Li, J.F., Wan, D., Huang, G.H., 2017a. Age, genesis, and tectonic setting of the Mo-W mineralized Dongshanwan granite porphyry from the Xilamulun metallogenic belt, NE China. J. Earth Sci. 28, 433–446.
Zhang, X.H., Zhang, H.F., Tang, Y.J., Wilde, S.A., Hu, Z.C., 2008b. Geochemistry of Permian bimodal volcanic rocks from Central Inner Mongolia, North China: implication for tectonic setting and Phanerozoic continental growth in Central Asian Orogenic Belt. Chem. Geol. 249, 262–281.
Zhang, X.N., Zeng, Q.D., Nie, F.J., 2022. Geochemical variations of the Late Paleozoic granitoids from the Baolidao arc-accrection belt in southeastern segment of Central Asia Orogenic Belt: implications for tectonic transition from Early Carboniferous to Early Permian. Journal of Earth Science 33 (3), 719–735.
Zhang, Y., Yang, J.H., Chen, J.Y., Wang, H., Xiang, Y.X., 2017b. Petrogenesis of Jurassic tungsten-bearing granites in the Nanling Range, South China: evidence from whole-rock geochemistry and zircon U-Pb and Hf–O isotopes. Lithos 278–281, 166–180.
Zhang, Z.J., Cheng, Q.M., Yao, L.Q., Bai, H.S., Li, C., 2016. Zircon U-Pb-Hf isotopic systematics and geochemistry of the granites in the Wurintu molybdenum deposit, Inner Mongolia, China: implications for tectonic setting and genetic type of mineralization. Acta Geol. Sin. (Eng. Ed.) 90, 2066–2079.
Zhao, G.C., Sun, M., Wilde, S.A., Li, S.Z., 2005. Late Archaean to Paleoproterozoic evolution of the North China Craton: key issues revisited. Precambrian Res. 136, 177–202.
Zhao, H.L., 2014. Ore genesis and Geodynamic Settings of Tungsten Deposits in Eastern Jilin and Heilongjiang Provinces [Ph.D. thesis]. Jilin University, Changchun (in Chinese with English abstract).
Zorin, Y.A., 1999. Geodynamics of the western part of the Mongol-Okhotsk collisional belt, Trans-Baikal region (Russia) and Mongolia. Tectonophysics 306, 33–56.